Viscoplastic behavior of a porous polycrystal with similar pore and grain sizes: application to nuclear MOX fuel materials

Luc Portelette, Pierre Guy Vincent, Hervé Moulinec, Mihail Garajeu

Viscoplastic behavior of a porous polycrystal with similar pore and grain sizes: application to nuclear MOX fuel materials

Luc Portelette
Aix Marseille Université, CNRS, Centrale Marseille, LMA, 13453 Marseille Cedex 13, France

Pierre-Guy Vincent
Institut de Radioprotection et de Sûreté Nucléaire, B.P. 3, 13115, Saint-Paul-lez-Durance Cedex, France
Laboratoire de Micromécanique et Intégrité des STructures, IRSN-CNRS-UM, B.P. 3, 13115, Saint-Paul-lez-Durance Cedex, France

Hervé Moulinec
Aix Marseille Université, CNRS, Centrale Marseille, LMA, 13453 Marseille Cedex 13, France

Mihail Gărăjeu
mihai.garajeu@univ-amu.fr (corresponding author)
Aix Marseille Université, CNRS, Centrale Marseille, LMA, 13453 Marseille Cedex 13, France

January 11, 2022

Abstract

This study deals with the viscoplastic behavior of a porous polycrystal with pores and grains of similar sizes. Such a microstructure can be encountered in irradiated nuclear Mixed OXide (MOX) fuel materials. MIcronized MASter blend (MIMAS) MOX are multi-phase materials mainly composed of two or three phases depending on their fabrication process. One of these phases corresponds to plutonium-rich agglomerates which strongly evolve during irradiation. The large Pu-rich agglomerates become highly porous due to the accumulation of fission gases and to the apparition of irradiation bubbles. In a past study, Wojtacki et al. (2020) showed that pores distributed inside the Pu-rich clusters have a strong impact on the overall viscoplastic behavior of MOX fuel, when considering a purely isotropic behavior for the Pu-rich clusters. In the present study, the impact of pores similar in size to the surrounding anisotropic grains on the overall viscoplastic behavior is studied in details through numerical full-field simulations. A crystal plasticity model recently developed by Portelette et al. (2018) is used to describe the anisotropic behavior of the polycrystalline matrix with dislocation glide mechanisms. Three-dimensional full-field simulations are performed by a method based on Fast Fourier Transforms (FFT) to compare the behavior of porous materials with that of dense materials. These simulations show that, in the case of spherical pores, their relative size with respect to that of the grains plays a minor role in the overall viscoplastic behavior. However, in the case of polyhedral pores, the relative size effect is more pronounced. With fixed porosity, decreasing the relative size of the cavities with respect to the size of grains leads to a softening of the material and a decrease of the viscoplastic flow stress.

Keywords: Porous media, Viscoplasticity, Polycrystal, Crystal plasticity, Fast Fourier Transform method, Nuclear MOX fuel

1 Introduction

This paper follows the previous work of Wojtacki et al. (2020) dedicated to the micromechanical modeling of viscoplastic porous materials with two rate-sensitivity exponents for an application to a Mixed OXide (MOX) fuel.

MOX fuel is a nuclear fuel made from plutonium oxide mixed with uranium oxide. It has notably been used in French Pressurised Water Reactors since 1987 (Oudinet et al., 2008). The manufacturing process of MOX fuel has a significant impact on the microstructure of the resulting material. The present study concerns MIcronized MASter blend (MIMAS)

Reference	σ [MPa]	T [°C]	O/M	d [μm]	ρ [%]	PuO_2 wt[%]	^{235}U [%]
Houston et al. (1970)	10-17	1100-1330	1.95-1.98	3-15	90-94	22	-
Evans et al. (1971)	7-70	1475-1625	1.95-2	4-23	88-94	0-100	-
Routbort et al. (1972)	7-110	1400-1675	1.83-1.99	10-47	95-97	25	65-93
Routbort and Voglewede (1973)	69	1500-1600	1.883-1.994	5-44	90-97	22/25	30-93
Slagle et al. (1984)	2.2-6.5	2175-2640	1.89-1.92	25	88-93	25	93
Caillot et al. (2004)	40-80	1535	-	5.5	95-96	6-10	-

Table 1: Creep tests on MOX pellets where σ is the compressive stress, T the temperature, O/M the oxygen-to-metal ratio, d the grain size, and ρ the pellet density.

MOX fuels. During the MIMAS process, a micronisation of a mixture with 25–30% plutonium dioxide is first performed, then followed by a dilution with natural or depleted uranium dioxide (White et al., 2001; Fisher et al., 2002). As a result, a material with plutonium-rich agglomerates is obtained. The uranium dioxide powders used in the process can be produced by AUC (Ammonium Uranate Carbonyl) or ADU (Ammonium DiUranate) routes leading to distinct microstructures. The MIMAS-AUC presents rather a two-phase microstructure with Pu-rich agglomerates and a matrix with a mixed content of uranium dioxide and plutonium dioxide. The MIMAS-ADU has rather a three-phase microstructure with Pu-rich agglomerates, a UO_2-rich matrix and a coating phase with intermediate Pu content (White et al., 2001). During irradiation, the large Pu-rich agglomerates become highly porous due to the accumulation of fission gases and to the apparition of irradiation bubbles (Noirot et al., 2008). Irradiation results in a variation of the physical properties of MOX fuel which is important to consider when estimating the loading applied by the fuel on the cladding, whose mechanical properties drastically change throughout their use in the reactor (see (Vincent et al., 2010) among others). The specific microstructure of MOX fuel and its evolution during irradiation must be studied closely to derive models for the thermo-mechanical behavior of MOX fuel during nominal or power transient operations, or under accident conditions, such as a Reactivity Initiated Accident (RIA) (Koo et al., 1997; Schmitz and Papin, 1999; Sasajima et al., 2000; Fuketa, 2012). The present study is devoted to the viscoplastic behavior of this fuel.

Earliest compression tests were conducted on UO_2 pellets for several temperatures, stresses, and strain rates (Byron, 1968; Bohaboy et al., 1969; Seltzer et al., 1970, 1971; Burton et al., 1973). These studies mainly highlighted two stationary creep regimes. For low stresses, the strain rate was observed to vary linearly with stress ($\dot{\varepsilon} \propto \sigma$). A point defect diffusion mechanism (together with a grain boundary sliding contribution) was attributed to this regime. For high stresses, the strain rate was observed to depend on the stress raised to a power close to 4.5 ($\dot{\varepsilon} \propto \sigma^{4.5}$). The dominant creep mechanism for this regime seemed to be the dislocation motion (dislocation glide and dislocation climb can occur). Then, creep tests were performed on MOX pellets (Houston et al., 1970; Evans et al., 1971; Routbort et al., 1972; Routbort and Voglewede, 1973; Slagle et al., 1984; Caillot et al., 2004) and, similarly to UO_2, two regimes were observed. Some features on the compression tests are reported in Table 1. Contrary to the tests performed on UO_2 pellets, the contents of Pu and ^{235}U are here systematically specified because they influence the mechanical behavior. Moreover, the tested materials reported in Table 1 remain understoichiometric. Stoichiometry is also known to influence their mechanical behaviors. Stresses are between 7 MPa and 110 MPa. Temperatures are between 1100°C and 1700°C, with the exception of (Slagle et al., 1984) in which tests are performed at temperatures higher than 2000°C, representative of extreme temperatures which could be encountered in a fuel during a postulated RIA (Suzuki et al., 2008).

From these studies, the unidimensional constitutive relation is classically written under the form:

$$\dot{\varepsilon} = A_1 \exp\left(-\frac{Q_1}{RT}\right)\sigma^{n1} + A_2 \exp\left(-\frac{Q_2}{RT}\right)\sigma^{n2}, \tag{1}$$

where $\dot{\varepsilon}$ and σ are respectively the strain rate and the creep stress along the compression direction. Parameters Q_i, n_i, and A_i are respectively the activation energy, the stress exponent and the prefactor for the ith mechanism (index $i = 1$ for point defect diffusion and $i = 2$ for dislocation motion). Some noticeable features of these parameters are reported in Table 2. The discrepancies observed on these parameters according to the different studies on MOX reported here are probably due to specimen selections, test conditions and experimental procedures. Nevertheless, the activation energies and stress exponents obtained from these studies remain close to each other, suggesting that they probably involve the same mechanisms. Moreover, it appears that the values obtained for MOX remain close to the values obtained for UO_2, probably indicating similar mechanisms involved. Furthermore, all these studies captured a grain-size dependency for the point defect diffusion mechanism, while no grain-size effect were found for the dislocation mechanism. Evans et al. (1971) identified a dependency as the inverse of the cube of the grain size and attributed that to interstitial diffusion in grain boundaries (Coble, 1963). The other authors found a dependency as the inverse of the square of the grain size and attributed that to vacancy diffusion in the grain bulk (Nabarro, 1948; Herring, 1950).

Later, compressive tests on UO_2 pellets were performed with higher stresses and strain rates (Guerin, 1975; Radford and Terwilliger, 1975; Tachibana et al., 1976; Salvo et al., 2015). From these studies, it was observed an increase of the stress exponent with stress, pointing out the presence of another deformation mechanism. The dislocation glide mechanism controlled by Peierls force was mentioned. Unfortunately, such tests were not conducted on MOX fuel. However, considering

MOX	A_1(d)	Q_1 [kcal.mol^{-1}]	n_1	A_2(d)	Q_2 [kcal.mol^{-1}]	n_2
Houston et al. (1970)	$\propto 1/d^2$	77	1.4	-	-	-
Evans et al. (1971)	$\propto 1/d^3$	100	1	-	140	4,5
Routbort et al. (1972)	$\propto 1/d^2$	92.5	1	-	136.8	4,4
UO_2						
Bohaboy et al. (1969)	$\propto 1/d^2$	90	1	-	132	4,5

Table 2: Parameters of the constitutive model (1).

the similarity between MOX and UO_2 fuels mentioned before, it is probable that the same deformation mechanism occurs for high stresses. The present study is focussed only on this gliding mechanism by extending the dislocation glide model developed for UO_2 (Portelette et al., 2018) to MOX polycristal.

MOX fuel is known to have a higher creep rate than UO_2 fuel which is an important feature when estimating the Pellet-Cladding Interaction (PCI) (Caillot et al., 2004). Furthermore, the porosities do not vary in the same way in the two fuels during irradiation and have a great impact on the viscoplastic behavior. In particular, irradiation and fission products help the development of pressurized bubbles surrounded by sub-grains. This is called the High Burn-up Structure (HBS). It is mainly located at the periphery of UO_2 fuel pellets (see (Lozano et al., 1998) among others) while it is mainly located at the large Pu-rich clusters in MOX fuels (Noirot et al., 2008). Noirot et al. (2008) showed that the size of bubbles and grains in the Pu-rich spots results from complex phenomena. Near the periphery of pellet (but not in the extreme periphery), where the temperature is lower in nominal conditions than at the center of the pellet, they observed on an irradiated MOX fuel, that the bubbles in Pu-rich clusters had approximately the same size than the surrounding sub-grains (mean values about 1.2 μm for the sub-grains and 1.3 μm for the bubbles). In the extreme periphery, bigger bubbles were observed and were attributed to higher burn-up in the agglomerates. At mid-radius, bubbles were approximately twice the size of sub-grains (mean values about 1.7 μm for the grains and 3 μm for the bubbles). At zero-radius, they observed very large bubbles (several tens of microns), though the grains sizes remained very similar to the initial sizes (about 7 μm). Therefore, irradiation conditions influence the relative size of the bubbles with respect to the size of grains. Thus, Noirot et al. (2008) clearly exhibited cases where bubbles and surrounding grains in Pu-rich clusters are similar in size. Fission gases exert internal pressure inside the bubbles, which consequently tends to round their shape. That's why, as a first approximation for modeling, one can consider spherical in shape bubbles. However it remains an approximation and deviations from the sphericity of the bubbles are therefore quite possible.

In a past study, Wojtacki et al. (2020) performed full-field simulations on periodic Representative Volume Elements (RVE) with an isotropic matrix, weakened by randomly distributed clusters of pores. The simulations were performed by a method based on Fast Fourier Transforms using the CraFT software (Suquet et al., 2012). This method, first proposed by Moulinec and Suquet (1994) is particularly effective when dealing with complex microstructures. In (Wojtacki et al., 2020), a random distribution of single-sized spherical clusters was used with single-sized pores randomly distributed inside the clusters. The porous clusters correspond to the large Pu-rich agglomerates in MOX fuel. The viscous strain in the matrix between the clusters and inside the clusters around the pores was described by two viscoplastic power-laws corresponding to two different creep mechanisms as described in equation (1) for MOX fuel. From these simulations, it was shown that the size of pores in the clusters has only a limited impact on the overall strain rate. The use of an isotropic viscoplastic behavior for the matrix surrounding the pores is legitimate when the cavities are larger than the surrounding grains and providing that the crystallographic orientation of the grains in the surrounding polycrystal be random. When cavities and grains have comparable sizes, the isotropy assumption is only motivated if the anisotropy introduced by the grains remains moderate. As stated above, the pores are subjected to internal pressure (P_b) due to the fission gas and the pores are said to be saturated. Wojtacki et al. (2020) only considered the case with a zero-pressure in the pores. In this case, the pores are said to be drained. This approach was motivated by a result demonstrated in (Vincent et al., 2009). In the case of an incompressible matrix, the macroscopic behavior in the saturated case can be obtained from the macroscopic behavior in the drained case by a simple shift along the axis of hydrostatic stresses. The macroscopic hydrostatic stress Σ_m obtained in the drained case is replaced by $\Sigma_m + P_b$ to treat the saturated case. This result is also used in the present study and only the drained case ($P_b = 0$) is considered without loss of generality. Note that this result applies when the material surrounding the pores is incompressible. In the present work, concerning the local behavior of the grains surrounding the pores, a compressible elastic part is added to the viscoplastic part which is incompressible. As a result, the local behavior of the grains is not purely incompressible. Nevertheless, the present study focusses on the response of the material deep into the plastic range, where the elastic effects become negligible compared to the viscoplastic effects and where the local behavior of the grains is close to the incompressibility.

The objective of the present study is to analyze the effect of the anisotropy due to the grains surrounding the pores on the overall viscoplastic behavior of MOX fuel (stationary creep). The particular case of pores and grains with similar sizes is studied. Two distinct shapes of pores are considered (spherical and polyhedral). The anisotropic behavior of the grains is modeled through a crystal plasticity constitutive relation (Portelette et al., 2018). Unlike Wojtacki et al. (2020), who considered simulations with several porous clusters embedded in a matrix, here, simulations are only performed on microstructures representative of porous clusters. FFT-based full-field simulations are performed on porous polycrystals.

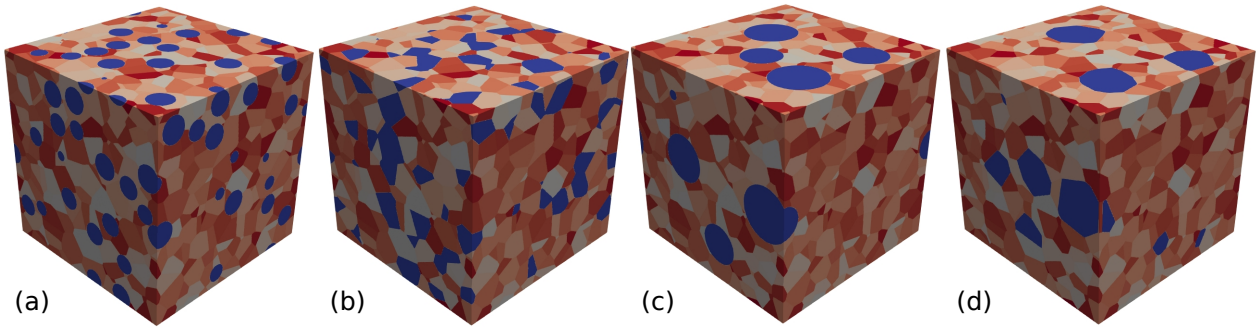

Figure 1: Periodic polycrystalline microstructures (500x500x500 voxels) with 15% porosity (voids in blue) (a) spherical voids with $d_p = d_g$, (b) polyhedral voids with $d_p \approx d_g$, (c) spherical voids with $d_p \approx 2\,d_g$, (d) polyhedral voids with $d_p \approx 2\,d_g$.

The paper is organized as follows. Section 2 presents the microstructures, the crystal plasticity model, and the loadings, together with some features about the FFT-based method used in the simulations. Results are shown in Section 3 and the main findings are discussed in Section 4.

2 Methods

2.1 Microstructure generation

In Pu-rich agglomerates near the pellet periphery, Noirot et al. (2008) found a case where bubbles and grains have approximately similar diameters. The estimated local burnup was about 100 GWd/t in this zone, which corresponds to a maximum volume fraction of pores in the agglomerates (f_p) of about 15%. Hence, in the present study, the simulations were performed on polycrystals with porosity varying from 0 (dense case) to 15%, by step of 5%. For the reason stated in the introduction, the pores were considered to be spherical in shape. However, this is just an approximation, therefore, an additional case was also studied, considering pores of polyhedral shape. Thus, the effect of the shape of pores could also be estimated. To identify the potential effect of the relative size of pores compared to the size of the grains, two different cases were treated:

- the diameter of the pores is approximately equal to the diameters of the grains, $d_p \approx d_g$,
- the diameter of the pores is approximately twice the diameters of the grains, $d_p \approx 2\,d_g$.

The arrangement of the grains is based on a Poisson-Voronoi diagram (Aurenhammer, 1991; Stoyan et al., 1995). A single set of $n_s = 1000$ seeds was considered in the whole study to generate the periodic polycrystals. In addition, a single set of grain orientations was also considered following a uniform random distribution. This follows from a parametric study reported in Appendix A on the statistical representativeness. The FFT scheme used in the present study requires a discretization of the unit cell with a regular grid composed of voxels. Based on the parametric study reported in Appendix A, a grid with 500^3 voxels has been adopted for all the simulations.

The average volume V_g of the grains in the Voronoi tessellation is thus given by V/n_s, where $V = 1$ is the volume of the unit cell. The average grain diameter d_g, defined as the diameter of an equivalent sphere of same volume V_g, is thus $(6\,V_g/\pi)^{1/3}$.

2.1.1 Spherical voids

To create the microstructures with spherical voids, single sized non-penetrable spheres were randomly positioned in the unit cell of the dense polycrystalline microstructure and all voxels inside the spheres were set to 0 (value corresponding to the void material, in blue in Figure 1). The number of pores (n_p) is determined from the desired volume fraction of pores and their relative size with respect to grains using the following relations:

$$f_p = \frac{n_p\,V_p}{V} = \frac{n_p}{n_s}\left(\frac{d_p}{d_g}\right)^3, \tag{2}$$

where V_p is the volume occupied by a pore. First, imposing $d_p = d_g$ leads to integer values of n_p, $n_p = n_s\,f_p = 1000\,f_p$. By doing so, a cell with 5% porosity and containing 50 pores will satisfy $d_p = d_g$. Thus, 10% porosity leads to 100 pores and 15% porosity leads to 150 pores. Secondly, imposing $d_p = 2\,d_g$ leads to $n_p = 125\,f_p$ and for the porosity values studied in this work (namely 5%, 10% end 15%) the value of n_p is not integer. We used instead $d_p = (10)^{1/3} d_g \approx 2\,d_g$ which leads to $n_p = 100\,f_p$. By doing so, a cell with 5% porosity and containing 5 pores will satisfy $d_p \approx 2\,d_g$. Thus, 10% porosity leads to 10 pores and 15% porosity leads to 15 pores. Some examples of microstructures with spherical voids are shown in Figures 1 (a) and (c). In the following, the microstructures obtained from this procedure are called Voronoi-type microstructures with spherical voids.

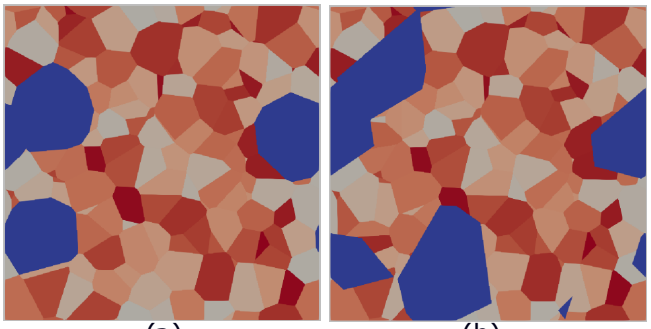

Figure 2: Slices of microstructures with 15% porosity, $d_p \approx 2\,d_g$ and polyhedral voids following (a) the procedure presented in 2.1.2, (b) the procedure presented in 2.1.3.

2.1.2 Polyhedral voids

For generating microstructures with polyhedral voids, some particular grains of the polycrystal were simply considered as void. They are called "voided grains" in the following.

Two different procedures were applied for generating such microstructures.

1. Depending on the targeted porosity, a given number of voided grains can simply be randomly selected among the grains of the initial dense polycrystal. This procedure can only be used if the same grain and pore sizes are desired ($d_p \approx d_g$). In the following, the microstructures obtained from this procedure are called Voronoi-type microstructures with polyhedral voids. Moreover, it does not guarantee to reach the exact volume fraction of pores desired, because of the statistical fluctuations of the grain sizes. To overcome these two limitations, a second procedure is proposed which makes use of Laguerre tessellations.

2. Laguerre tessellations, also called power diagrams, are an extension of Voronoi tessellations where the euclidian distance - used in Voronoi tessellation to determine for each point of the volume which is the closest seed - is replaced by the "power distance" (Aurenhammer, 1987; Lautensack and Zuyev, 2008). Alternatively, Laguerre tessellations can be considered as the result of the crystal growth process where a set of seeds are positionned in space and time - each seed s is thus determined by the couple $(\boldsymbol{x_s}, t_s)$ - and where each crystal grows from its corresponding seed with a constant growth rate G of the square of their distance to its seed, untill it reaches another crystal. In other words, a given point $\boldsymbol{x}$ is reached by the growth of crystal s at time $t = d^2(\boldsymbol{x}, \boldsymbol{x_s})/G \; + \; t_s$ (where $d(,)$ denotes the euclidian distance), and at the end, $\boldsymbol{x}$ belongs to the crystal which reaches it first. As for the Voronoi tessellations, the cells of the Laguerre tessellations are convex polyhedra, but the choice of the times t_s at which the crystals start to grow, and of the growth rate G enables to drive the sizes of the resulting cells. In the particular case where all the values of t_s are equal, the resulting tessellation is a Voronoi diagram.

   In order to obtain microstructures with similar voids distribution as the Voronoi-type microstructures with spherical voids we proceed in two steps. Firstly, the grains of the initial dense polycrystal (with $n_s = 1000$ grains) which contain the centers of the spherical voids are selected. The seeds of these grains will be the seeds of the voided grains. Then the procedure applied in this study consists in fixing the nucleation time t_s of the seeds of the voided grain to 0, and the nucleation time of the other grains to 1, and in searching the growth rate in order to reach the desired volume fraction with the following algorithm:

   - the first estimate of the surface growth rate G is set arbitrarily,
   - if it does not lead to the desired volume fraction, an extrapolation is made to define the next value,
   - then, for the next iterations, G is estimated by interpolating the values already calculated, until the volume fraction of pores is reached (with a precision set to 10^{-4}).

   In the following, the microstructures obtained from this procedure are called Laguerre-type microstructures with polyhedral voids.

Some examples of microstructures with polyhedral voids are shown in Figure 1 (b) and (d) and in Figure 2 (a).

2.1.3 Additional microstructures

For further discussions (section 4.1), two additional kinds of microstructures were generated.

The first one is a polycrystal with spherical voids obtained by a slightly different method from that described in section 2.1.1. First, a Laguerre-type microstructure with polyhedral voids is considered. Second, the voided grains are replaced by

Name	Void shape	Tessellation	Note
Voronoi-type microstructures with spherical voids	spherical	Voronoi	only for $d_p \approx d_g$
Voronoi-type microstructures with polyhedral voids	polyhedral	Voronoi	uncontrolled porosity
Laguerre-type microstructures with polyhedral voids	polyhedral	Laguerre	
Additional microstructures			
Voronoi-type microstructure with re-centered spherical voids	spherical	Laguerre	Laguerre tessellation for the voids Voronoi tessellation for the grains
Laguerre-Voronoi-type microstructures with polyhedral voids	polyhedral	Laguerre/Voronoi	

Table 3: Main features for the different microstructures of the study.

dense grains and spherical pores of identical sizes are centered at the barycenters of these selected grains. In the following, this microstructure is called Voronoi-type microstructure with re-centered spherical voids.

The second one consists in generating a new set of positions of grain seeds, where the number of seeds n_s is set to n_p/f_p. Some of these seeds are randomly selected to be the seeds of the voided grains. The number of voided grains is set as in 2.1.1. A Laguerre tessellation is then performed and the algorithm described above is used to get the desired volume fraction of porosity. All the voided grains thus obtained are then superimposed on the initial dense polycrystalline microstructure with 1000 grains. This lead to unrealistic microstructures because the faces of the voids do not depend on the surrounding grains (see Figure 2 (b)). In the following, the microstructures obtained by this procedure are called Laguerre-Voronoi-type microstructures with polyhedral voids.

To sum up, the main features for the different types of microstructures are summarized in Table 3.

2.2 Crystal plasticity model

By lack of single-crystal experiments available for MOX fuel, the crystal plasticity model of Portelette et al. (2018), initialy proposed for UO_2 single crystals, is used to describe the behavior of the grains. This assumption is motivated by the fact that MOX and UO_2 fuels exhibit a fairly similar overall viscoplastic behavior. Moreover, PuO_2 and UO_2 have the same fluorite lattice structure.

Here, viscoplasticity is driven by the glide of dislocations on crystallographic planes, identified by their normal vectors $\boldsymbol{n}^s$. During the slip process, a shear strain is produced along directions $\boldsymbol{m}^s$ colinear to Burgers vectors of type $1/2\langle 110\rangle$. Each pair $[m^s](n^s)$ defines a slip system. In a fluorite lattice, there are three families of slip systems given by different slip plane symmetries, usually named family *I*, *II* and *III* and corresponding to {100} slip planes, {110} slip planes and {111} slip planes, respectively. Therefore, there are 24 slip systems with 6 systems for family *I*, 6 systems for family *II*, and 12 systems for family *III*. Since in UO_2 the role of the third family seems to be less significant and is not yet very well understood, it is not considered in this study (see (Portelette et al., 2018) for more details). Detailed expressions of $\boldsymbol{n}^s$ and $\boldsymbol{m}^s$ vectors can be found in (Portelette et al., 2020).

The Cauchy stress tensor $\boldsymbol{\sigma}$ is related to the elastic strain tensor $\boldsymbol{\varepsilon}^e$ through the fourth-order elastic tensor $\boldsymbol{C}$:

$$\boldsymbol{\sigma} = \boldsymbol{C} : \boldsymbol{\varepsilon}^e. \tag{3}$$

The elastic strain tensor $\boldsymbol{\varepsilon}^e$ is obtained from the difference between the total strain, $\boldsymbol{\varepsilon}$, and the viscoplastic strain, $\boldsymbol{\varepsilon}^{vp}$:

$$\boldsymbol{\varepsilon}^e = \boldsymbol{\varepsilon} - \boldsymbol{\varepsilon}^{vp}. \tag{4}$$

The viscoplastic strain rate is the sum of the slip rates, $\dot{\gamma}^s$, projected on each slip system s using the symmetric Schmid tensor $\boldsymbol{\mu}^s_{sym}$:

$$\dot{\boldsymbol{\varepsilon}}^{vp} = \sum_{s=1}^{12} \dot{\gamma}^s \boldsymbol{\mu}^s_{sym} = \overbrace{\sum_{s=1}^{6} \dot{\gamma}^s \boldsymbol{\mu}^s_{sym}}^{\{100\}} + \overbrace{\sum_{s=7}^{12} \dot{\gamma}^s \boldsymbol{\mu}^s_{sym}}^{\{110\}}, \tag{5}$$

$$\boldsymbol{\mu}^s_{sym} = \frac{1}{2}(\boldsymbol{n}^s \otimes \boldsymbol{m}^s + \boldsymbol{m}^s \otimes \boldsymbol{n}^s). \tag{6}$$

The evolution of the slip rate in each slip system s, is given by equation (7). To account for the temperature dependency, T, an activation energy, ΔH^i_0, is defined for each slip family i. Note that the dependence of the slip rate on the stress is

	1/2<110>{100}	1/2<110>{110}
$\dot{\gamma}_0$ [s^{-1}]	5.22×10^8	1.52×10^8
ΔH_0 [eV]	5.71	5.22
τ_0 [MPa]	4.86	17.2

Table 4: Parameters of the crystal plasticity model.

modelled by a hyperbolic cosine function. For each slip system family, a prefactor $\dot{\gamma_0}^i$ is introduced as a parameter, together with a reference resolved shear stress denoted by τ_0^i:

$$\dot{\gamma}^s = \dot{\gamma}_0^i \exp\left(-\frac{\Delta H_0^i}{k_b T}\right)\left(\cosh\left(\frac{\tau^s}{\tau_0^i}\right) - 1\right)\text{sign}(\tau^s). \tag{7}$$

Here, $k_b = 8.618\,10^{-5}$ eV.K^{-1} is the Boltzmann constant. The resolved shear stress τ^s is defined as the projection of the stress on the slip system s:

$$\tau^s = \boldsymbol{\sigma} : \boldsymbol{\mu}^s_{sym}. \tag{8}$$

The above constitutive equations were implemented in the CraFT software (Suquet et al., 2012). Details on the time-integration of the equations are given in Appendix B.

For each slip family, the three parameters ($\dot{\gamma}_0^i$, ΔH_0^i, τ_0^i) are adjusted in order to match with the experiments of Routbort et al. (1972) conducted on MOX fuel in the dislocation motion regime (see Appendix C for details). The obtained parameters are specified in Table 4. The elastic anisotropy is accounted for by assuming a cubic stiffness tensor $\boldsymbol{C}$. The evolution of the three elastic constants (C_{11}, C_{12}, and C_{44} in Voigt notations) with temperature are obtained by interpolations between the experimental results of Wachtman et al. (1965). The introduction of an elastic part is useful for the time-integration of the constitutive equations (see Appendix B). Since the present study concerns the overall viscoplastic behavior, only the overall stress obtained at the end of the simulation is kept, when the elasticity effects become negligible (loadings specified in 2.4).

Even if Portelette et al. (2018) considered finite strains, here, the constitutive equations are implemented under the small strain assumption, since the maximum strain investigated is rather low. In addition, both studies do not consider the isotropic hardening due to dislocation interactions. Indeed, Portelette et al. (2020) determined the coefficients of the interaction matrix and it is shown in (Portelette, 2018) that such hardening in a thermally-activated regime of dislocation glide is not relevant in UO_2.

Note that, since the size of pores considered here is above a few microns (see section 1 about the microstructure of irradiated MOX fuel), the surface effects predominant for nanosized inclusions are not considered here (Haller et al., 2015, 2016).

2.3 FFT-based homogenization method

The numerical simulations presented in this study are carried out using the CraFT code (Suquet et al., 2012). This software is based on a full-field numerical method, introduced by Moulinec and Suquet (Moulinec and Suquet, 1994, 1998), which allows the calculation of the homogenized mechanical quantities of a given heterogenous material from the data of its microstructure and the properties of its constituents.This method basically consists in solving the Lippmann-Schwinger equation and makes an intensive use of Fast Fourier Transforms (FFT). A major feature of the method is that it relies on a discretization of the space according to a regular grid, *i.e.* on spatial data organized in the form of two- or three-dimensional images made of pixels or voxels. Thus, the microstructural data are provided by an image of the material, making possible the direct use of experimental results obtained by imaging techniques. The method was designed for numerical efficiency and has proven to converge mostly much faster in terms of spatial discretization than the more classical FEM-based methods on similar problems (El Shawish et al., 2020).

Following Joëssel et al. (2018) and Vincent et al. (2020) on porous viscoplastic crystals and polycrystals, the numerical scheme used in the particular context of this study is a fixed-point iterative scheme (called "basic scheme" by some authors). The convergence criterion is here the one introduced by Bellis and Suquet (2019) which proved to be the most suitable mathematically.

2.4 Loadings

The overall stress (also called effective or macroscopic stress) is denoted by $\boldsymbol{\Sigma}$ and the overall strain is denoted by $\boldsymbol{E}$. The effective response of dense polycrystal with the model presented in Section 2.2, is in good agreement with the experiments in the dislocation mechanism domain as shown in Appendix C. Therefore, in this study, the investigated temperature range was taken from 1400°C to 1700°C and the strain-rate range was from 10^{-7} s^{-1} to 10^{-4} s^{-1}.

The triaxiality diagram was explored using mechanical tests with imposed overall stress direction and controlled overall strain in the stress direction (see Appendix B in (Moulinec and Suquet, 1998) for more details). Note that this procedure

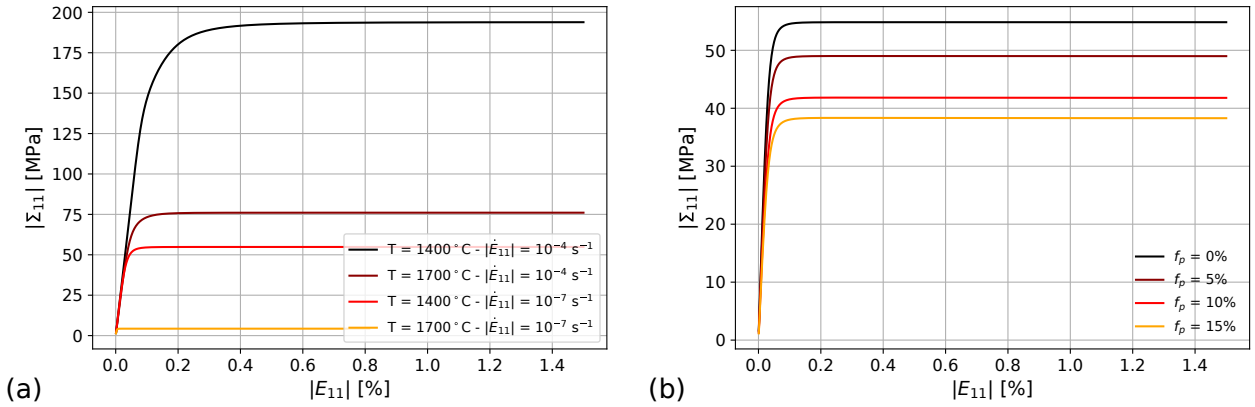

Figure 3: Macroscopic stress versus macroscopic strain in the compression direction (absolute values) during a uniaxial compression loading (a) on the dense polycrystal for different temperatures and strain rates, (b) on the dense polycrystal and Voronoi-type microstructures with polyhedral voids for $d_p \approx d_g$, $T = 1400°\text{C}$, and $|\dot{E}_{11}| = 10^{-7}$ s^{-1}.

is extremely useful to test the response of heterogeneous porous cells under different loading paths (as done here with the FFT based method), but also to test the response of analytical macroscopic models for porous media derived from a micromechanical approach on a material point (see for example (Nkoumbou Kaptchouang et al., 2021)).

Several overall stress triaxialities were prescribed to investigate the effect of porosities considering the first and the second stress invariants, i.e. the hydrostatic stress, Σ_m, defined in equation (9) and the Von Mises equivalent stress defined in equation (10), in which the deviatoric stress tensor is defined by $\boldsymbol{\Sigma}^d = \boldsymbol{\Sigma} - \Sigma_m \boldsymbol{I}$ and $\boldsymbol{I}$ is the second-order identity tensor. The overall stress triaxiality is then defined by the ratio of the two invariants: $T_\sigma = \Sigma_m / \Sigma_{eq}$. Note that the effect of the third stress invariant was not studied here.

$$\Sigma_m = \frac{1}{3} tr\left(\boldsymbol{\Sigma}\right), \tag{9}$$

$$\Sigma_{eq} = \sqrt{\frac{3}{2} \boldsymbol{\Sigma}^d : \boldsymbol{\Sigma}^d}. \tag{10}$$

An axisymmetric overall stress direction, $\boldsymbol{\Sigma}_0$, was prescribed:

$$\boldsymbol{\Sigma}_0 = \begin{bmatrix} -1 & 0 & 0 \\ 0 & c & 0 \\ 0 & 0 & c \end{bmatrix}, \tag{11}$$

where, c is a scalar between -1 and 0.5 dedicated to control the stress triaxiality. Uniaxial compression tests (corresponding to the case where $T_\sigma = -1/3$ and $c = 0$) were performed in order to allow a comparison with experimental results reported in the literature. Moreover, purely deviatoric ($T_\sigma = 0$, $c = 0.5$) and purely hydrostatic compressions ($T = -\infty$, $c = -1$) tests, corresponding to the two extreme triaxialities, and two intermediate tests (($T_\sigma = 1$, $c = -0.4$) and ($T_\sigma = 3$, $c = -0.7273$)) were performed to cover the whole domain of triaxiality.

For all cases investigated, it was chosen to deform until the projected strain, $|E| = |\boldsymbol{E} : \boldsymbol{\Sigma}_0|$, reaches 1.5%. This value allows to estimate the asymptotic overall stress with reasonable accuracy. Uniaxial and deviatoric simulations were performed with 1500 constant time steps while 2500 to 3000 time steps were used for hydrostatic simulations, because numerical convergence is harder to achieve in hydrostatic case than for deviatoric and uniaxial loadings. The overall hydrostatic stress and the overall equivalent stress obtained at the end of the simulations are checked so that they vary less than 0.1 MPa in the last 100 time steps.

Tables D.1 and D.2 in appendix D summarize all the simulations achieved for each microstructure and loading.

3 Results

3.1 Uniaxial compression loading

Let us consider the case of uniaxial compression loading as defined in 2.4 (imposed direction of overall stress). Figure 3 (a) shows some stress-strain curves obtained on the dense polycrystal. As expected, the stress level deep in the plastic range decreases with the temperature and increases with the strain rate. The effect of porosity on the strain-stress curves at 1400°C and 10^{-7} s^{-1} is illustrated in Figure 3 (b). Voronoi-type microstructures with polyhedral voids are here considered. As expected, the pores induce a softening of the material and the stress level deep in the plastic range decreases with porosity.

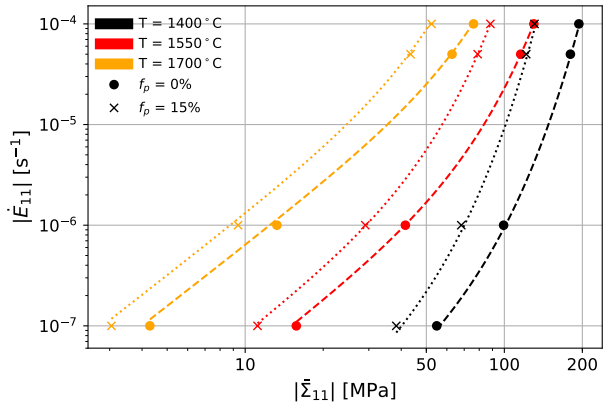

Figure 4: Strain rate versus stress for different temperatures obtained on the dense polycrystal and Voronoi-type microstructures with polyhedral voids and $d_p \approx d_g$. Uniaxial compression loading.

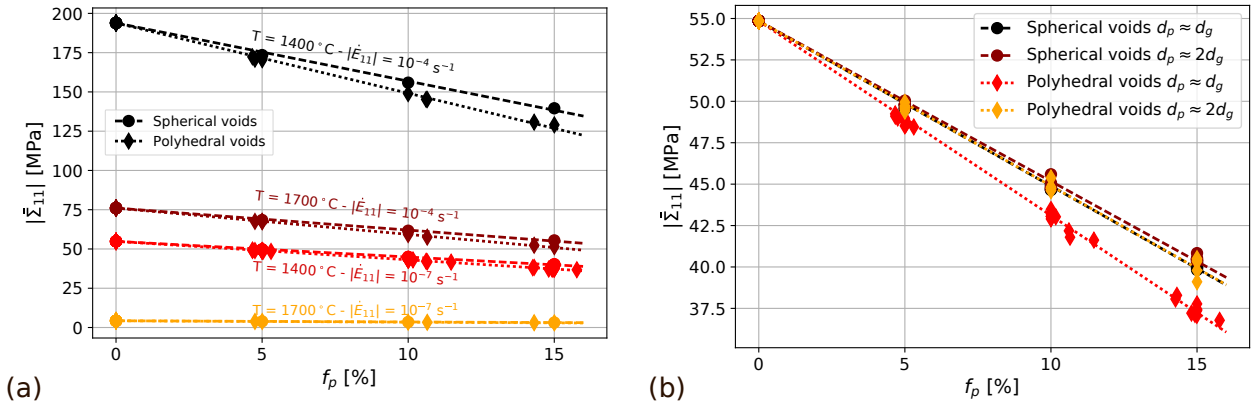

Figure 5: Stress versus porosity for Voronoi-type microstructures with spherical voids, Laguerre-type and Voronoi-type microstructures with polyhedral voids, submitted to a uniaxial compression loading (dotted and dashed lines are linear regression functions). (a) $d_p \approx d_g$ for different temperatures and strain rates, (b) $d_p \approx d_g$ and $d_p \approx 2\,d_g$ for $T = 1400$°C and $|\dot{E}_{11}| = 10^{-7}$ s^{-1}.

In the following, the macroscopic stress obtained at the end of the computation is denoted by $\bar{\boldsymbol{\Sigma}}$ (its component along the compression direction is $\bar{\Sigma}_{11}$). Figure 4 shows that the dependence of stress on strain rate is not linear in a log-log representation. Here, a hyperbolic cosine function is used to fit the evolution of the strain rate, $|\dot{E}_{11}|$, with the stress, $|\bar{\Sigma}_{11}|$, for each temperature T (dashed lines in Figure 4):

$$|\dot{E}_{11}| = A \exp\left(-\frac{Q}{RT}\right)\left(\cosh\left(\frac{|\bar{\Sigma}_{11}|}{\Sigma_0}\right) - 1\right) \tag{12}$$

where $R = 8.314$ J.mol^{-1}.K^{-1} is the gas constant. Here, a better fit is obtained with a hyperbolic cosine function than with an exponential or a hyperbolic sine function which are more often used in the literature. The parameters, determined by a least squares regression, are the prefactor $A = 9.68 \times 10^8$ s^{-1}, the activation energy $Q = 539$ kJ.mol^{-1} (or $\Delta H_0 = 5.59$ eV), and the referential stress $\Sigma_0 = 20.5$ MPa. Note that theses values are close to the values for family I and II reported in Table 4. The effect of porosity observed in a log-log representation (Figure 4) exhibits a global softening compared to the dense material, no matter the temperature and the strain rate. By adjusting the equation (12), the parameters with 15% porosity are $A = 1.58 \times 10^9$ s^{-1}, $Q = 549$ kJ.mol^{-1} and $\Sigma_0 = 13.5$ MPa. Therefore, porosity markedly affects the prefactor and the referential stress while the activation energy does not change significantly. This means that porosity facilitates the dislocation motion but faintly influences the temperature dependency.

Figure 5 (a) shows the evolution of the stress —$\bar{\Sigma}_{11}$— with respect to the porosity f_p for some values of temperature and strain rate. Microstructures with similar in size pores and grains are considered. Voronoi-type microstructures with spherical voids, Laguerre-type microstructures with polyhedral voids, and Voronoi-type microstructures with polyhedral voids are considered. An almost linear evolution of the stress with respect to the porosity is observed. The dashed and dotted lines are linear functions adjusted by a least squares regression to highlight the trends for microstructures with spherical voids and polyhedral voids respectively. The slope is steeper at lower temperature and at higher strain rate. It appears that the simulations with polyhedral voids systematically induce more softening than the simulations with spherical voids.

Results for microstructures with $d_p \approx d_g$ and $d_p \approx 2\,d_g$ are presented for 1400° C and 10^{-7} s^{-1} in Figure 5(b). First, it appears that the stress discrepancies due to the different draws of microstructures remain low for both relative size of pores and microstructures investigated. The discrepancies appear slightly higher for the microstructures with polyhedral voids than for microstructures with spherical voids. Also, the discrepancies obtained from the different draws of a given type of microstructure increase with the relative size of pore. Indeed, increasing the relative size of pore tends to decrease the number of pores in the unit cell, which induces a loss of representativeness. Nevertheless, the level of discrepancies remains relatively small showing a sufficient representativeness. Secondly, results obtained from Laguerre-type and Voronoi-type microstructures with polyhedral voids (described in Section 2.1.2) lie on the same interpolated line. Note that the porosity is not perfectly controlled for Voronoi-type microstructures with polyhedral voids, because of statistical fluctuations during the generation process. Thus, in Figure 5, the points associated with these microstructures correspond to porosities slightly scattered with respect to the desired porosities (5, 10 or 15%). This outlines the equivalence of the two ways of generating the microstructures with polyhedral voids. Thirdly, when the relative size of voids increases, the stresses obtained from the microstructures with polyhedral voids tend to the stresses obtained from the microstructures with spherical voids. To the end, it is observed that the effect of the relative size of voids with respect to the size of grains is negligible for microstructure with spherical voids (less than 1 MPa absolute difference and less than 1% relative differences). It appears to be more pronounced for microstructures with polyhedral voids (maximum relative difference about 5%).

3.2 Other loading conditions

Figure 6 shows the macroscopic equivalent stress as a function of the macroscopic hydrostatic stress obtained at the end of the simulations for different macroscopic stress triaxialities. Voronoi-type microstructures with spherical voids and Laguerre-type microstructures with polyhedral voids are considered. The strain rate $\dot{E}$ is given by $\dot{\boldsymbol{E}} : \boldsymbol{\Sigma}_0$ where $\boldsymbol{\Sigma}_0$ is the imposed direction of macroscopic stress. In Figure 6 (a), it is observed that the higher the stress triaxiality (in absolute value), the higher the difference between the stresses for the sets of temperature and strain rate studied. From Figure 6 (b), it appears that the softening observed in uniaxial compression due to porosity is also noticeable for other loading conditions and increases with the stress triaxiality. In addition, the effect of the type of pores (spherical or polyhedral in shape) is also enhanced with stress triaxiality. Finally, it is observed in Figure 6 (c) that the effect of the relative size of pores remains small for microstructures with spherical voids for all the stress triaxialites investigated. For microstructures with polyhedral voids, it is more pronounced and it increases with stress triaxiality. Furthermore, when $d_p \approx 2\,d_g$, the behavior for the microstructures with polyhedral voids tends to be similar to the behavior of the microstructures with spherical voids.

As explained at the end of the section 4.1, for polyhedral voids, increasing the relative size leads to voids which are closer to the spherical shape. This could be the reason why the curves in Figure 6 (c) corresponding to spherical voids and to polyhedral voids with $d_p \simeq 2\,d_g$ are close to each other. In line with these arguments, the differences observed on curve corresponding to the polycrystal with polyhedral voids with $d_p \simeq d_g$, compared to the other curves, especially for high stress triaxiality, seem to be an effect of the shape of the cavities rather than a size effect.

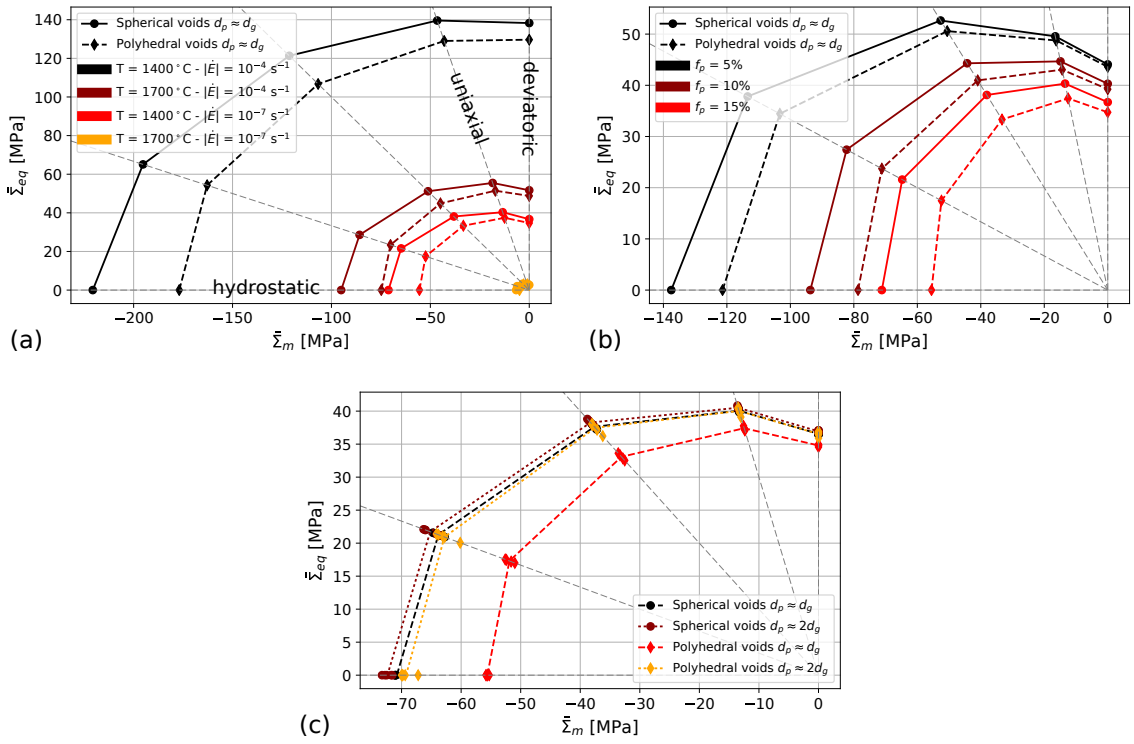

Figure 6: Equivalent stress versus hydrostatic stress of Voronoi-type microstructures with spherical voids, Laguerre-type microstructures with polyhedral voids (dotted and dashed lines are interpolations between the mean values obtained for each stress triaxiality) (a) for different temperatures and strain rates with $d_p \approx d_g$ and $f_p = 15\%$, (b) for different porosities with $d_p \approx d_g$, $T = 1400°\text{C}$, and $|\dot{E}| = 10^{-7}$ s^{-1}, (c) for $d_p \approx d_g$ and $d_p \approx 2\,d_g$ with $f_p = 15\%$, $T = 1400°\text{C}$, and $|\dot{E}| = 10^{-7}$ s^{-1}.

4 Discussion

4.1 Crystallinity and pore shape effects

In this study, it is observed that the relative size of pores with respect to the size of grains has a minor effect on the overall viscoplastic behavior in the case of spherical voids. Thus, in this case, the material seems insensitive to the crystallinity and the anisotropy of the grains surrounding the pores. This is in accordance with (Lebensohn et al., 2011), in which the numerical simulations and theoretical predictions for the viscoplasticity of polycrystalline solids containing intergranular spherical voids (grains and cavities with a similar size) indicate that the effective response of untextured voided solids was relatively insensitive to the crystallinity of the matrix.

It is observed in the present study, that the effect of the relative size of pores with respect to the size of grains on the overall viscoplastic behavior is quite pronounced for microstructures with polyhedral voids and negligible for microstructures with spherical voids. Wojtacki et al. (2020) observed a negligible increase of the strain rate for a constant porosity when the size of pores is decreasing. Their observation were based on simulations of creep tests on a material with an isotropic viscoplastic matrix and spherical pores organized into clusters representative to irradiated MOX fuel. Boittin et al. (2017) studied the effect on the effective plastic flow surface of the relative size of intergranular lenticular cavities located along grain boundaries with respect to the mean grain size in a biporous material with spherical intragranular cavities. An isotropic matrix surrounding the intergranular lenticular cavities was considered. For a constant volume fraction of intergranular bubbles, the effective yield stress was found to reduce when decreasing the relative size of the bubbles. This effect was larger for a purely hydrostatic overall stress direction than for a purely deviatoric axisymmetric overall stress direction. These observations were in good agreement with those of Bilger et al. (2005) who carried out simulations of porous media composed of a perfectly plastic matrix with connected clusters of voids.

Figure 7 shows maps of equivalent strain obtained at the end of the simulation for a Voronoi-type microstructure with re-centered spherical voids (see section 2.1.3) and a Laguerre-type microstructure with polyhedral voids under hydrostatic compression. The equivalent strain seems highly localized in zones between neighboring voids. For both microstructures, a strong interaction between neighboring voids is thus obtained, which is in line with the results of Lebensohn et al. (2011) for purely hydrostatic loading. Nevertheless, it appears that the spatial distribution of the equivalent strain at the extreme periphery of the voids is quite different considering spherical or polyhedral voids (see black circles in Figure 7). In some zones around the polyhedral voids, the equivalent strain may remain very low and in other zones around the polyhedral voids it may experience large values. In the case of spherical voids, a non-zero equivalent strain is typically observed all around the

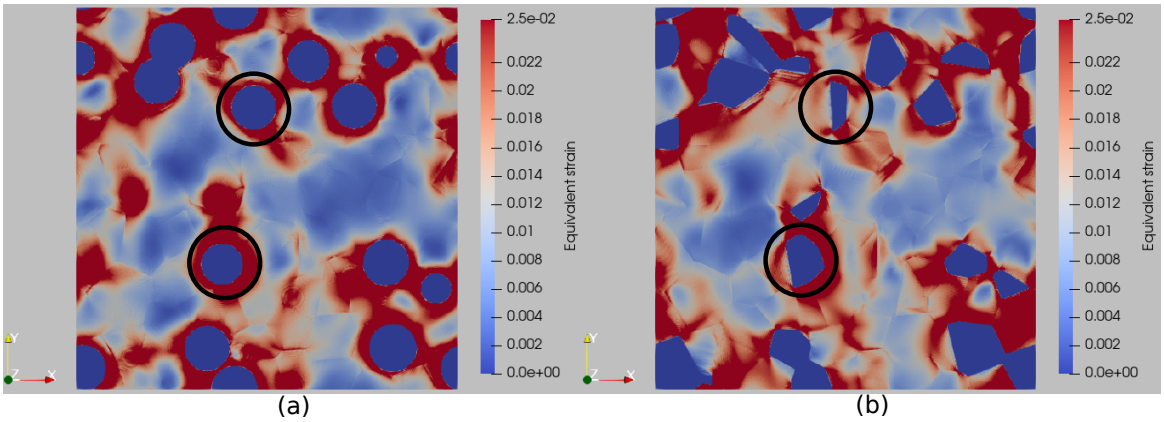

Figure 7: Equivalent strain fields at the end of the simulation for $f_p = 15\%$ under hydrostatic compression with $d_p \approx d_g$, $T = 1400°\text{C}$, and $|\dot{E}| = 10^{-7}$ s^{-1}. (a) Voronoi-type microstructure with re-centered spherical voids (see section 2.1.3), (b) Laguerre-type microstructure with polyhedral voids. Isovalues are bounded with a maximum value set to 2.5%. In microstructures (a) and (b), pore centers have identical positions.

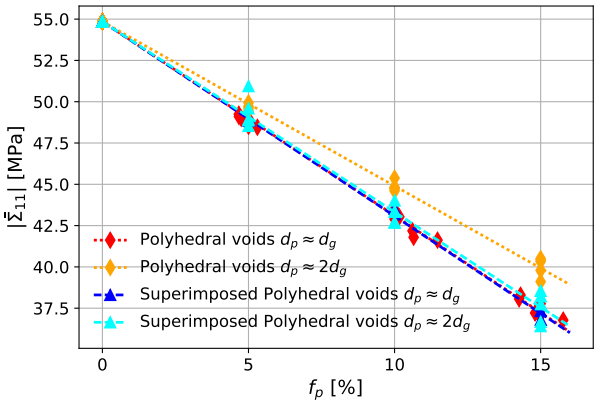

Figure 8: Stress versus porosity for $T = 1400°\text{C}$ and $|\dot{E}_{11}| = 10^{-7}$ s^{-1}. Voronoi-type and Laguerre-type microstructures with polyhedral voids (red). Laguerre-type microstructures with polyhedral voids (orange). Laguerre-Voronoi-type microstructures with polyhedral voids (dark blue and light blue). Dotted and dashed lines are linear fit functions.

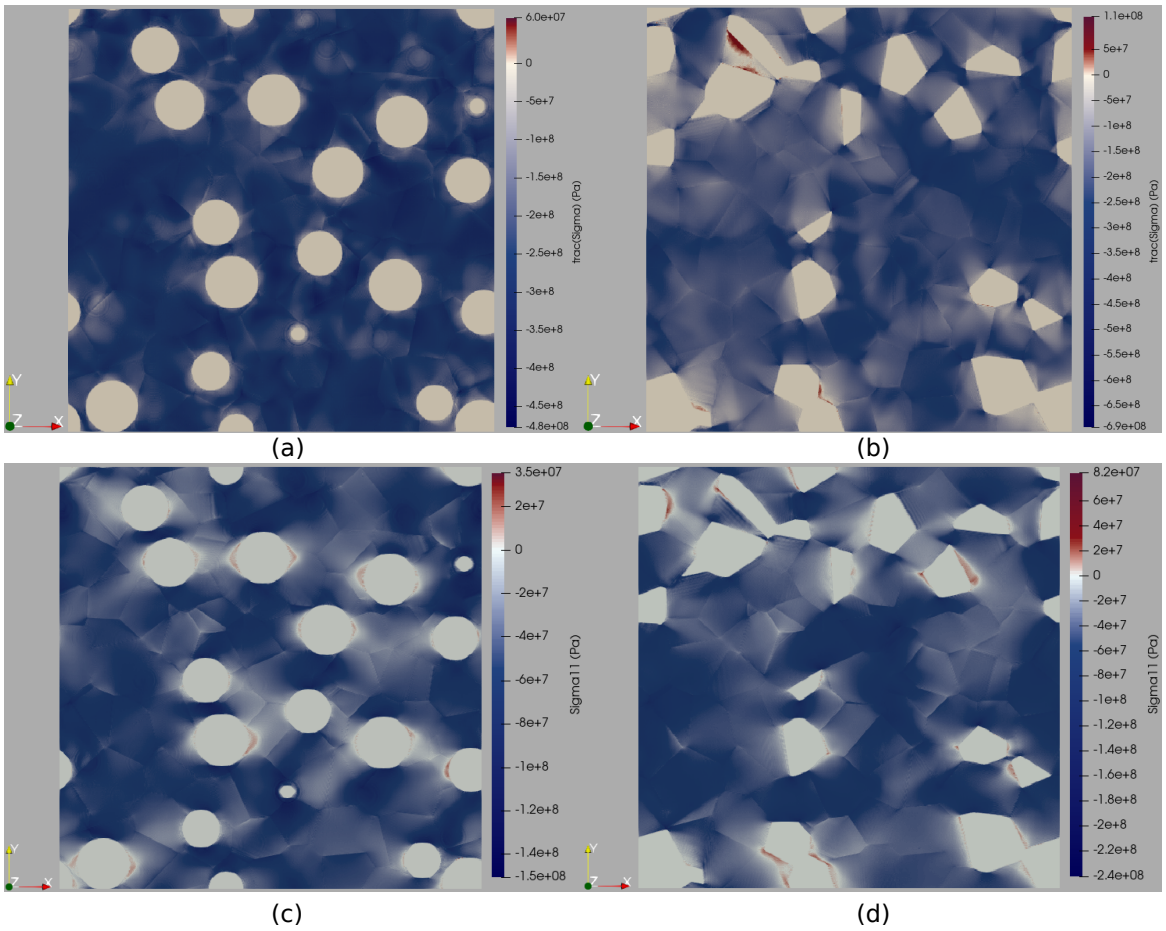

Figure 9: Stress fields at the end of the simulation for $f_p = 15\%$. $d_p \approx d_g$, $T = 1400°C$, and $|\dot{E}| = 10^{-7}$ s^{-1}. Hydrostatic compression, maps of $tr(\boldsymbol{\sigma})$ (a) for a Voronoi-type microstructure with spherical, (b) for a Laguerre-type microstructure with polyhedral voids. Uniaxial compression, maps of σ_{11} (c) for a Voronoi-type microstructure with spherical voids, (d) for a Laguerre-type microstructure with polyhedral.

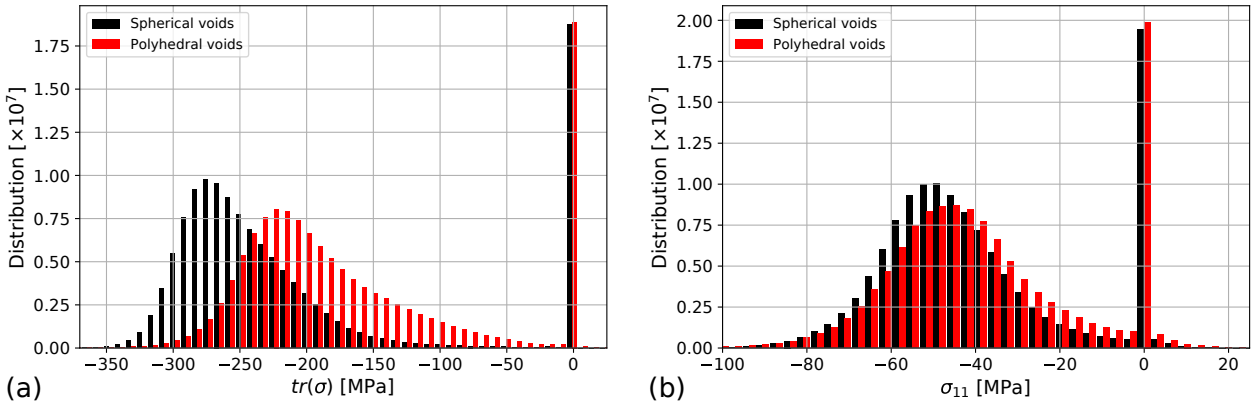

Figure 10: Distribution of stress at the end of the simulation for $f_p = 15\%$ in Voronoi-type microstructure with spherical voids and Laguerre-type microstructure with polyhedral voids. $d_p \approx d_g$, $T = 1400°C$, and $|\dot{E}| = 10^{-7}$ s^{-1}. (a) $tr(\boldsymbol{\sigma})$ for hydrostatic compression loading, (b) σ_{11} for uniaxial compression loading.

cavities. Thus, it appears that the shape of the pores has an influence on the local fields.

Here, when $d_p \approx d_g$, it is observed that the stresses obtained from microstructures with polyhedral pores are lower than the stresses obtained from microstructures with spherical pores. Nevertheless they are not generated with the same process. In one hand, the microstructures with spherical voids are generated by superimposing spherical cavities on an initial Voronoi tessellation. In the other hand, the microstructures with polyhedral voids are directly generated from a Voronoi or Laguerre tessellation (some cells of the tessellation are considered as voids). As a result, we investigate whether this difference in results is caused by the difference in the building process, one with overlap and the other without. Thus, an additional type of microstructures is considered with polyhedral voids (see Figure 2 and Section 2.1.3) with a superposition of cavities obtained from a Laguerre tessellation directly mapped onto a Voronoi tessellation. Figure 8 shows the results obtained from Voronoi-type and Laguerre-type microstructures with polyhedral voids under uniaxial compression (as in Figure 5), together with the results obtained from this additional type of microstructures with polyhedral voids. When $d_p \approx d_g$ it is observed that the different types of microstructures lead to similar results. It shows that the difference in the building process, with or without overlap cannot explain the difference in results obtained from microstructures with polyhedral and spherical pores. Moreover, Figure 8 shows that the results obtained from the additional microstructures with polyhedral pores are not very sensitive to the relative pore size (similar results for $d_p \approx d_g$ or $d_p \approx 2\,d_g$). Thus the additional microstructures with polyhedral voids lead to a negligible size effect, unlike the other microstructures with polyhedral voids. Note that the polyhedral voids in the additional microstructures have larger and fewer facets than the voids in the Laguerre-type microstructures with polyhedral voids when $d_p \approx 2\,d_g$ (see Figure 2). It could explain the specific behavior observed on these additional microstructures. Consequently, it indicates that the difference between results obtained on microstructures with polyhedral and spherical pores when $d_p \approx d_g$ mentioned above is probably due to the shape of pores.

To better understand the pore shape effect, local stress fields are shown in Figure 9 for hydrostatic and uniaxial compression loadings and for both types of microstructures. Note that the color bar is set to visualize the minimum and maximum values of stresses in the two microstructures and the color gradient is adjusted to get approximately the same colors for the same values around 0 MPa. The dispersion is larger in the case of polyhedral voids than spherical voids. For hydrostatic loading, the zones with small values of local hydrostatic stress are more spread in the case of the polyhedral voids than spherical voids. Even if it is less noticeable for the uniaxial loading, it seems that the same trend is emerging for the local stress in the compression direction. This means that the polyhedral void case contains more unloaded zones than the spherical void case. To quantify these differences, distributions of stresses are plotted in Figure 10. The peak observed at 0 MPa is mainly due to the stress-free voids. As expected, the spread of small stresses is larger in the case of the microstructure with polyhedral voids, especially under hydrostatic compression with a clear shift of the distribution. For uniaxial compression, the shift is less pronounced, but the amount of voxels with small stresses is clearly larger for the microstructure with polyhedral voids. Thus, it seems that the differences obtained on the microstructures with the two types of pore are due to the spread of small stress zones around the pores.

The non-spherical shape effect was largely discussed in the literature, first in 2D (Zimmerman, 1986; Kachanov et al., 1994; Tsukrov and Novak, 2002; Ekneligoda and Zimmerman, 2006), showing that the overall compressibility in elasticity depends on the ratio of the square of the perimeter of pores over its surface area. Thus, they highlighted that the circular pore shape is the stiffest in 2D, since it gives the lowest perimeter for a given surface area. In 3D, many authors investigated the pore shape effect, considering regular pore shapes (Sevostianov and Giraud, 2012; Sevostianov et al., 2016; Chen et al., 2015, 2018; Markov et al., 2020; Du et al., 2020, 2021) or irregular pore shapes (Drach et al., 2011, 2014, 2016; Markov et al., 2020). In a similar way to 2D, the ratio of the surface area of pores over their volume is of great importance for the overall compressibility in elasticity. This is well in line with the results of the present study, since the surface area of polyhedral pores is larger than the surface area of spherical pores of same volume. Furthermore, the fact that the discrepancy between the results obtained with Voronoi-type microstructure with spherical pores and those of Laguerre-type microstructures with polyhedral pores is reduced when $d_p \simeq 2\,d_g$ compared to the one of the case when $d_p \simeq d_g$ (see Figure 6 (c)), can be explained by the more spherical aspect of the pores when $d_p \simeq 2\,d_g$, which is well illustrated in Figure 1 (b) and (d). Oppositedly, as can be seen in 8, the Laguerre-Voronoi-type microstructures with polyhedral voids, with either $d_p \simeq d_g$ or $d_p \simeq 2\,d_g$ have a mechanical response close to that of Laguerre-type microstructures with polyhedral voids with $d_p \simeq d_g$, probably because the shapes of the pores in the two cases are very similar - they only differ in their sizes - and thus present the same deviation to sphericity.

4.2 Modified porosity

From Figure 5, it seems that the case of polyhedral voids and $d_p \approx d_g$ can be derived from the case of spherical voids by multiplying the porosity by a constant q (to be determined). It could serve to extend the analytical model developed in (Wojtacki et al., 2020) for spherical voids to polyhedral voids when the size of voids is similar to the size of grains. Multiplying the porosity by q in this analytical model could lead to an estimate when the pores are polyhedral with a size close to the size of grains. Since porosity have the highest influence in hydrostatic loadings, q is determined from the evolution of the hydrostatic stress with the porosity for hydrostatic loadings. Then the value of q is used, with no further fitting, to simulate the uniaxial tests and the purely deviatoric tests at different strain-rate levels and different temperatures.
The overall hydrostatic stress at the end of the simulation versus porosity for microstructures with $d_p \approx d_g$ under hydrostatic compression is presented in Figure 11 (c) for different temperatures and strain rates. The evolution of overall hydrostatic

T [°C]	$\lvert\dot{E}\rvert$ [s^{-1}]	T_σ	Spherical voids		Polyhedral voids		q_{sv}			
			A_{sv}	B_{sv}	A_{pv}	B_{pv}	5%	10%	15%	mean
1400	10^{-4}	-∞	-156.6	643.5	-167.1	626.4	1.24	1.30	1.34	1.29
		-1/3	-3.7	193.8	-4.5	193.8				
		0	-3.3	186.5	-3.9	186.5				
1400	10^{-7}	-∞	-77.1	302.9	-79.7	286.7	1.30	1.33	1.35	1.33
		-1/3	-1.4	76.0	-1.7	76.0				
		0	-1.1	68.5	-1.3	68.5				
1700	10^{-4}	-∞	-60.7	234.8	-60.5	218.1	1.31	1.30	1.30	1.30
		-1/3	-0.99	54.9	-1.17	54.9				
		0	-0.77	48.1	-0.90	48.1				
1700	10^{-7}	-∞	-7.6	27.0	-7.2	24.2	1.33	1.28	1.25	1.29
		-1/3	-0.08	4.3	-0.09	4.3				
		0	-0.05	3.5	-0.06	3.5				

Table 5: Parameters of equations (13) and (14) identified by a least squares regression and q values determined from equation (16).

stress with porosity is estimated for spherical voids and polyhedral voids respectively using the following relation:

$$|\bar{\Sigma}_m| = A_i \, \ln(f_p) + B_i. \tag{13}$$

where i is the type of pore ('sv' for spherical voids and 'pv' for polyhedral voids). The logarithm function is inspired from the hollow sphere problem with Von Mises rigid plastic matrix under purely hydrostatic loading in the original Gurson analysis (Gurson, 1977). The coefficients A_i and B_i are determined using a least squares regression (see Table 5).
In Figures 11 (a) and (b), it is observed that the evolutions of $\bar{\Sigma}_{eq}$ and $|\bar{\Sigma}_{11}|$, respectively for purely deviatoric and uniaxial compression loadings, with porosity are quite linear. Therefore, they are estimated by:

$$|\bar{\Sigma}_{eq,11}| = A_i \, f_p + B_i. \tag{14}$$

The parameters A_i and B_i identified by the least squares regression are reported in Table 5 for both types of microstructure.
In Figure 11 (c), dashed and dotted lines correspond to the evolution of stress as a function of porosity for spherical voids and polyhedral voids respectively using the following relation:

$$|\bar{\Sigma}_m| = A_i \, \ln(q_i \, f_p) + B_i. \tag{15}$$

The parameter q_{sv} is adjusted for spherical voids to meet the relation for polyhedral voids where $q_{pv} = 1$:

$$q_{sv} = \frac{1}{f_p} \exp\left(\frac{A_{pv} \log(f_p) + B_{pv} - B_{sv}}{A_{sv}} \right). \tag{16}$$

A mean value for q_{sv} is computed for each set of temperature and strain rate in Table 5. The obtained values are then averaged, leading to $q_{sv} = 1.3$. It is checked in Figure 11 (c) that the dashed lines with $q_{sv} = 1.3$ (simply denoted by q) remain close to the dotted lines for the different temperatures and strain rates.
In Figures 11 (a) and (b), dashed and dotted lines correspond to the evolution of stress as a function of porosity for spherical voids and polyhedral voids respectively using the following relation:

$$|\bar{\Sigma}_{eq,11}| = A_i \, (q_i \, f_p) + B_i. \tag{17}$$

with $q_{sv} = 1.3$ and $q_{pv} = 1$. The dashed lines with $q_{sv} = 1.3$ (simply denoted by q) slightly underestimates the results for the microstructures with polyhedral voids. Nevertheless, the discrepancies remain below 5% of the stress for both loadings.

5 Conclusions

Porous polycrystalline microstructures with similar in size pores and grains are generated to analyze the effect of the anisotropy due to the grains surrounding the pores on the overall viscoplastic behavior. Such microstructures can be encountered in large Pu-rich clusters of irradiated MOX fuels. Two distinct shapes of pores are considered (spherical and polyhedral), together with two relative sizes of the voids with respect to the grains. Specific algorithms are derived to generate the different microstructures of Voronoi and Laguerre tessellations. The local deformation of the grains is assumed to follow a crystal plasticity law recently developed for UO_2 and adjusted here to fit with experimental results on MOX fuel. Full-field simulations using a Fast Fourier Transforms based method are performed imposing the direction of the overall stress.

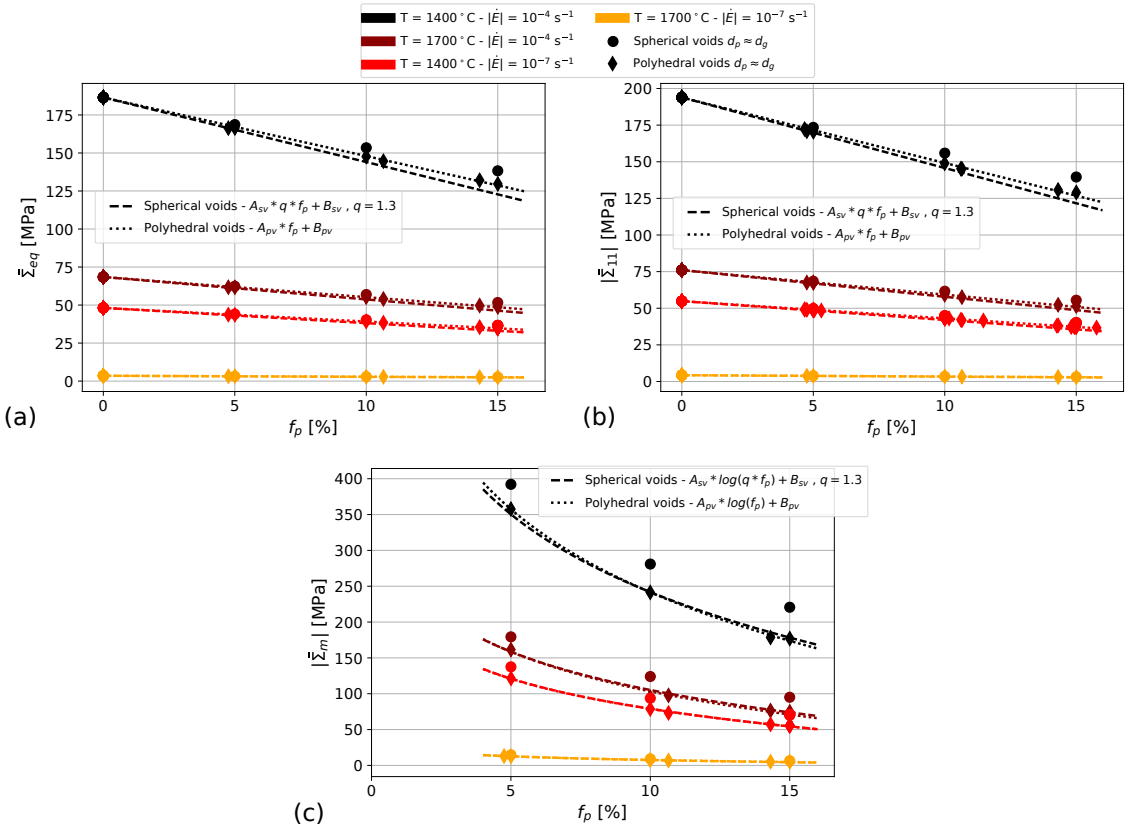

Figure 11: Stress versus porosity for different temperatures and strain rates and $d_p \approx d_g$ for Voronoi-type microstructures with spherical voids, Laguerre-type and Voronoi-type microstructures with polyhedral voids under (a) purely deviatoric loading, (b) uniaxial compression loading, (c) purely hydrostatic compression loading.

Different overall stress triaxilities are considered, corresponding to uniaxial compression, purely hydrostatic compression, and purely deviatoric axisymmetric loadings. To the end, the results are obtained from a massive computation plan, varying the temperature, the strain rate, the porosity, the pore shape, the relative size of pores with respect to the grains, and the stress triaxiality. As expected, the porosity has a softening effect on the effective viscoplastic behavior. The effect of the relative size of pores remains small for microstructures with spherical voids for all the stress triaxialities investigated, thus indicating a minor effect of the crystallinity and the anisotropy of the grains on the overall viscoplastic response.

For further investigations, the effect of crystallinity should be assessed when additional local processes are taken into account, such as lattice rotation, strain hardening due to interactions between dislocations or between dislocations and point defects, or processes implying point defects diffusion, or dislocation climb. Coming from the fact that the crystal plasticity model is local, another limitation of this study could be that it does not take into account the possible effect of geometrically necessary dislocations induced by large strain gradients around the pores.

For microstructures with polyhedral voids, the effect of the relative size of pores is more pronounced and it increases with stress triaxiality. Furthermore, when the relative size of pores with respect to the size of grains increases, the behavior of the microstructures with polyhedral voids tends to the behavior of the microstructures with spherical voids. It seems that the difference between results obtained on microstructures with polyhedral and spherical pores is due to the shape of pores itself, leading to different spreads of small stress zones around the pores. It is shown that the case of polyhedral voids when the size of voids is equal to the size of grains can be derived with good accuracy from the case of spherical voids by multiplying the porosity by a constant $q \approx 1.3$. It could be used to extend the analytical model developed in (Wojtacki et al., 2020) for MOX fuel with spherical pores. Multiplying the porosity by q in this analytical model gives an estimate when the pores are polyhedral with a size close to the size of grains.

Acknowledgments

Some of the full-field simulations presented here were made possible thanks to the resources of the CCRT (Centre de Calcul Recherche et Technologie) of the CEA/DIF. The authors are grateful to J. Noirot for several remarks concerning the high burn-up structure of MOX fuel.

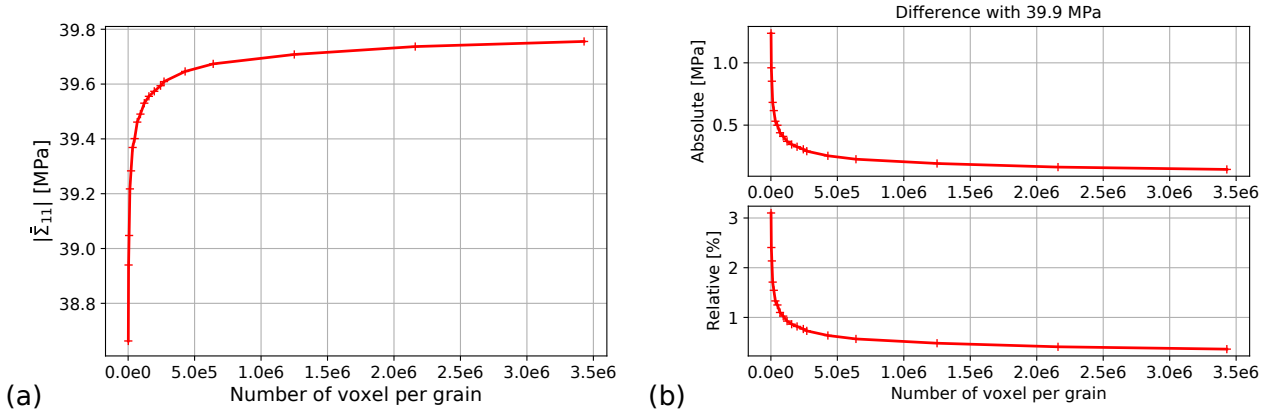

Figure A.1: (a) Effective stress on a 100 grains Voronoi-type microstructure with 15 polyhedral voids, at 1900°C and 10^{-3} s^{-1}, under uniaxial compression. (b) Absolute and relative differences of each simulation results with 39.9 MPa.

A Parametric studies

A.1 Spatial discretization

Spatial discretization, which can be defined as the number of voxels/pixels per volume element, plays an important role on the accuracy of the calculation performed with FFT-based homogenization method. First, a high spatial discretization enables a fine description of the microstructure (and thus a simulation closer to the physical problem). Second, it enables a better estimate of the mechanical fields and the overall material properties.

To study the influence of spatial discretization, several simulations were performed on a canonical microstructure, considering the viscoplastic behavior of the material and the porosity. A microstructure composed of 85 viscoplastic crystals and 15 voided grains (Voronoi-type microstructure with polyhedral voids generated as described in 2.1.2) was subjected to a uniaxial compression test, with a strain rate of $10^{-3}s^{-1}$ (see the description of the loadings in Section 2.4), at a temperature set to 1900°C, for a spatial discretization varying from 1,250 to 3,430,000 voxels per grain. To be more specific, the discretization is defined here as the total number of voxels in the image, divided by the total number of grains, voided or not, in the volume.

The results are summarized in Figure A.1. It appears that the effective stress obtained at the end of the simulation converges toward an asymptotic value with an increasing spatial discretization (Figure A.1 (a)) and that the asymptotic value is nearly reached with the largest investigated discretization. The resuts are compared here to a reference value set to 39.9 MPa, which overestimates the value obtained with the highest resolution. Figure A.1 (b) shows that the difference between the calculated overall stress and this reference value is below 0.5 MPa, which corresponds to a relative difference of 1%, for spatial discretization over 100,000 voxels per grain.

To conclude, a spatial discretization of 125,000 voxels per grain has been retained for this study.

A.2 Macroscopic isotropy and representativeness

The goal of this parametric study is to determine the minimal number of grains in the unit cell of a dense polycrystal required to get, with a good accuracy, a macroscopic isotropic mechanical response.

Eight classes of microstructures were considered which contained 10, 70, 100, 250, 400, 700, 1000 and 1500 grains, respectively, with a discretization of 125,000 voxels per grain. For each class, 30 realizations were generated. Examples of microstructures used in this study are presented in Figure A.2, for different numbers of grains.

Each cell was tested under three loading conditions corresponding to uniaxial compressions along the three directions of the space. The temperature was set to 1400°C and the unit cell was loaded with constant overall strain rate (of 10^{-4} s^{-1}) until 1.5% of the corresponding overall axial strain was reached (see the description of the loadings in Section 2.4).

In Figure A.3 are compared the average values (over all realizations) of the effective uniaxial stresses obtained at the end of the simulations along the three directions of the space as functions of the number of grains. As expected, the standard deviation of the results within each class of microstructures decreases with the number of grains and it is less than 2,5% for classes containing more than 250 grains. For unit cells containing more than 700 grains these average values are visually indistinguishable.

Thus, it is reasonable to consider that a unit cell containing more then 700 grains is quite representative and gives an almost isotropic mechanical effective response. The numerical simulations presented in this paper are performed on unit cells containing 1000 grains.

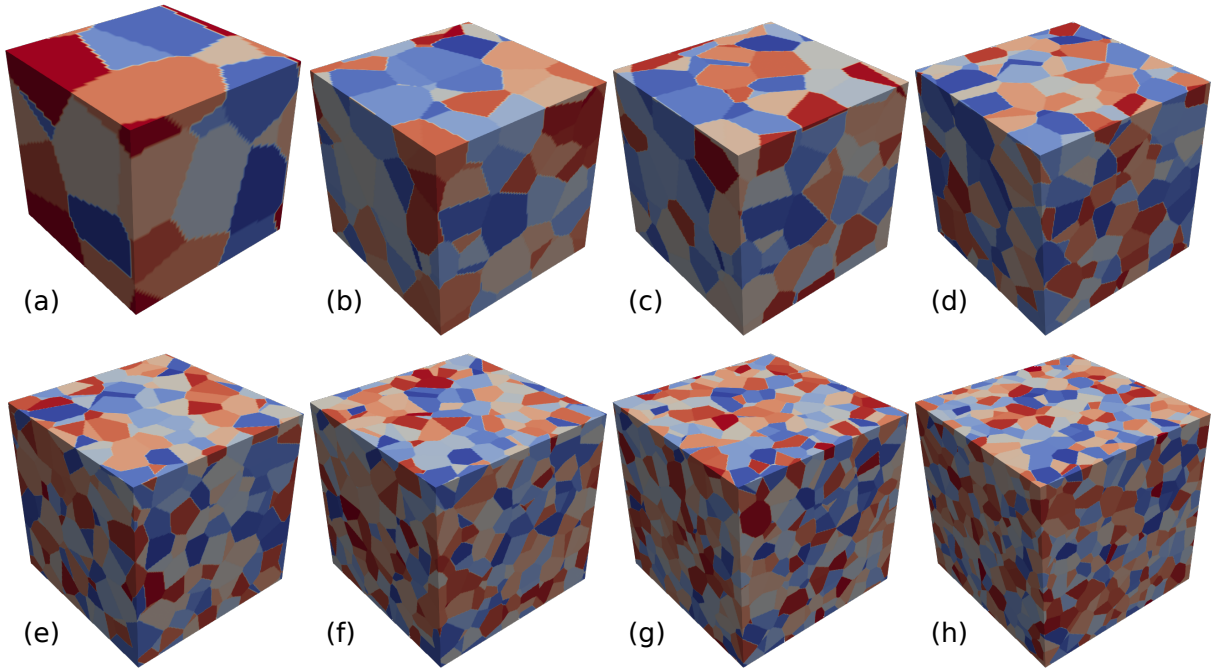

Figure A.2: Microstructures of dense polycrystal for different number of grains: (a) 10 grains, (b) 70 grains, (c) 100 grains, (d) 250 grains, (e) 400 grains, (f) 700 grains, (g) 1000 grains, and (h) 1500 grains.

B Integration of the crystal plasticity model in CraFT

The crystal plasticity model introduced in 2.2 and used in this study can be summarized by the following set of constitutive equations:

$$\begin{cases} \dot{\boldsymbol{\sigma}} = \boldsymbol{C} : (\dot{\boldsymbol{\varepsilon}} - \dot{\boldsymbol{\varepsilon}}^{vp}) \\ \dot{\boldsymbol{\varepsilon}}^{vp} = \sum_s \dot{\gamma}^s \boldsymbol{\mu}^s_{sym} \\ \dot{\gamma}^s = \dot{\gamma}^i_0 \exp\left(-\dfrac{\Delta H^i_0}{k_b T}\right) \\ \qquad\qquad \left(\cosh\left(\dfrac{\tau^s}{\tau^i_0}\right) - 1\right) \operatorname{sign}(\tau^s) \\ \tau_s = \boldsymbol{\sigma} : \boldsymbol{\mu}^s_{sym} \\ \boldsymbol{\mu}^s_{sym} = \dfrac{1}{2}(\boldsymbol{n}^s \otimes \boldsymbol{m}^s + \boldsymbol{m}^s \otimes \boldsymbol{n}^s) \end{cases} \tag{B.1}$$

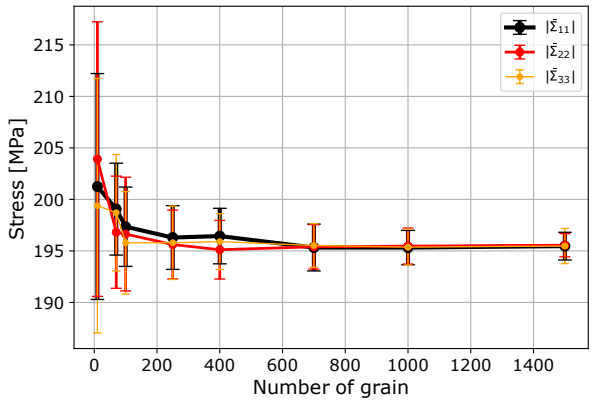

Figure A.3: Effective uniaxial average stresses over all microstructure realizations containing the same number of grains, at the end of the simulations along the three directions of the space versus the number of grains at 1400°C and 10^{-4} s^{-1}. Bars indicate the standard deviation.

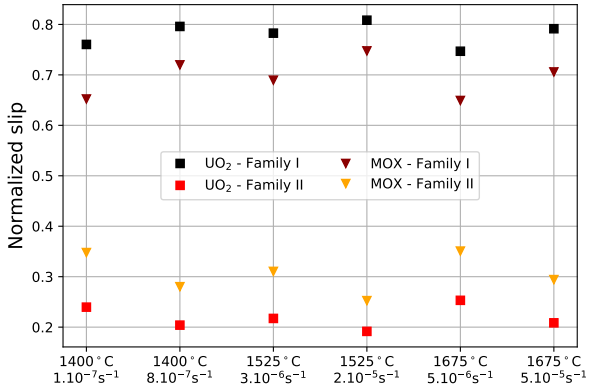

Figure C.1: Normalized slip (equations (C.1) and (C.2)) of the two slip families of UO_2 and MOX for different temperatures and strain rates.

This model has been integrated in time in CraFT code by introducing a time increment Δt and by discretizing the stress rate and the strain rate in time as follows:

$$\begin{aligned} \dot{\boldsymbol{\sigma}} &= \frac{\boldsymbol{\sigma}(t) - \boldsymbol{\sigma}(t-\Delta t)}{\Delta t}, \\ \dot{\boldsymbol{\varepsilon}} &= \frac{\boldsymbol{\varepsilon}(t) - \boldsymbol{\varepsilon}(t-\Delta t)}{\Delta t}\ . \end{aligned} \tag{B.2}$$

Thus, by developing (B.1), the following equation is obtained:

$$\boldsymbol{F}(\boldsymbol{\sigma}(t)) = \boldsymbol{0}, \tag{B.3}$$

with

$$\begin{aligned} \boldsymbol{F}(\boldsymbol{\sigma}(t)) = \quad & \boldsymbol{\sigma}(t) - \boldsymbol{\sigma}(t-\Delta t) - \boldsymbol{C} : \big(\boldsymbol{\varepsilon}(t) - \boldsymbol{\varepsilon}(t-\Delta t)\big) \\ + \Delta t \sum_s \Bigg[\quad & \dot{\gamma}_0^i \exp\Big(-\frac{\Delta H_0^i}{k_b T}\Big)\Bigg(\cosh\Big(\frac{\boldsymbol{\mu}_{sym}^s : \boldsymbol{\sigma}(t)}{\tau_0^i}\Big) - 1\Bigg) \\ & \operatorname{sign}(\boldsymbol{\mu}_{sym}^s : \boldsymbol{\sigma}(t)) \ \ \boldsymbol{C} : \boldsymbol{\mu}_{sym}^s \Bigg], \end{aligned}$$

where the only unknown is the current stress $\boldsymbol{\sigma}(t)$, the current strain $\boldsymbol{\varepsilon}(t)$ and the strain $\boldsymbol{\varepsilon}(t-\Delta t)$ and the stress $\boldsymbol{\sigma}(t-\Delta t)$ at the previous time step being supposed to be known.

Equation (B.3) is solved iteratively using the Newton-Raphson method.

C Parameters of crystal plasticity model for MOX fuel

In this study, the crystal plasticity model developed by (Portelette et al., 2018) for UO_2 is used for MOX fuel. The two materials have the same fluorite lattice structure and a similar viscoplastic behavior. However, the parameters of the model should be adjusted in order to match with the experimental results. Since no experimental data are available for MOX single crystal, we use experimental measurements obtained by Routbort et al. (1972) on MOX pellets in the dislocation motion regime.

The three parameters $\dot{\gamma}_0^i$, ΔH_0^i and τ_0^i, of each slip family, are adjusted by comparing the experimental results with the results of numerical simulations. The simulations were performed on the dense polycrystal. The unit cell containing 1000 grains was submitted to a uniaxial compression and the effective axial stress is determined for different temperatures and strain rates.

In both materials (UO_2 and MOX) the viscoplastic strain-rate is the sum of the slip rates, $\dot{\gamma^s}$, on each slip system. In order to preserve the same mechanism for the evolution of the viscoplastic strain-rate in the two materials, when adjusting the parameters mentioned before, we have kept the dominance of the slips of the family I compared to the ones of the family II. To evaluate it, the sum of slips of each family is normalized by the sum of slips of all slip systems (equations (C.1) and (C.2)):

$$\frac{\gamma^I}{\gamma^{tot}} = \frac{\sum_{s=1}^{6} \gamma^s}{\sum_{s=1}^{12} \gamma^s}, \tag{C.1}$$

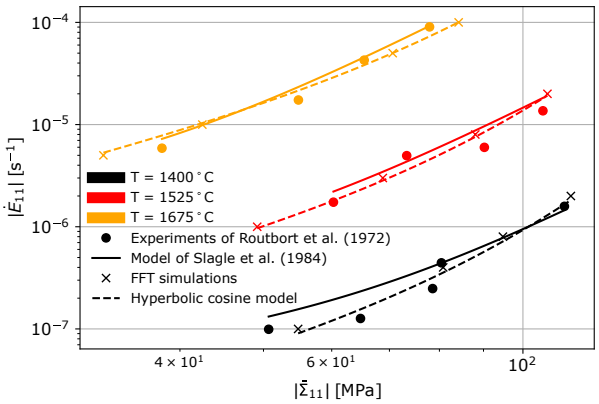

Figure C.2: Comparison between Routbort et al. (1972) experiments (circles), simulations on the dense polycrystal (crosses), model of Slagle et al. (1984) with parameters specified by Wojtacki et al. (2020) (solid line) and hyperbolic cosine model (equation (12) - dashed line) for three temperatures.

$$\frac{\gamma^{II}}{\gamma^{tot}} = \frac{\sum_{s=7}^{12} \gamma^s}{\sum_{s=1}^{12} \gamma^s}. \tag{C.2}$$

In Figure C.1 are reported these ratios for both materials and for different temperatures and strain rates. The choice of the parameters which is presented hereafter, ensure that the normalized slip of family I is always greater than the normalized slip of family II for all temperatures and all strain rates.

After several tries a good choice found of these parameters is the following:

- the values of ΔH_0^i are kept unchanged for both slip families,
- the values of τ_0^i are 3.6 times larger than the corresponding values for UO_2 for both slip families,
- the values of γ_0^i for family 1/2¡110¿100 are 11 times larger than the corresponding values for UO_2,
- the values of γ_0^i for family 1/2¡110¿110 are 22 times larger than the corresponding values for UO_2.

It is worth noting that the procedure for adjusting these parameters is purely heuristic and other set of parameters could give similar results.

In Figure C.2 are compared the experimental results of Routbort et al. (1972) with the results of the FFT simulations for three temperatures. The predictions of the model of Slagle et al. (1984) with the parameters specified in (Wojtacki et al., 2020), and the hyperbolic cosine model (equation (12)) are also plotted. The results of the numerical simulations show that, at least for the range of strain rates considered here, the set of parameters identified previously for the MOX fuel leads to an effective behavior which is close to the one observed in experiments, for the whole range of temperature. We can also remark that the model of Slagle et al. (1984) accurately predicts the behavior of the dense polycrystal.

D Simulation cases

Tables D.1 and D.2 summarized all the simulation cases performed on Voronoi-type microstructures with spherical voids and Laguerre-type microstructures with polyhedral voids. Moreover, the simulations performed on the other types of microstructures are indicated in these tables:

- the simulation on the Voronoi-type microstructure with re-centered spherical voids is added in the column 'Spherical voids' with $d_p \approx d_g$ and is indicated in parentheses (.),
- simulations on Voronoi-type microstructures with polyhedral voids are added in the column 'Polyhedral voids' with $d_p \approx d_g$ and are indicated in braces {.},
- simulations on Laguerre-Voronoi-type microstructures with polyhedral voids are added in the column 'Polyhedral voids' and are indicated in square brackets [.].

				Spherical voids		Polyhedral voids	
T [°C]	$\lvert\dot{E}\rvert$ [s^{-1}]	f_p [%]	T_σ	$d_p \approx d_g$	$d_p \approx 2d_g$	$d_p \approx d_g$	$d_p \approx 2d_g$
1400		0	-1/3			1	
	10^{-7}	5	0	1		1+{1}	
		5	-1/3	5	5	5+{5}+[5]	5+[5]
		5	-1	1		1	
		5	-3	1		1	
		5	-∞	1		1+{1}	
		10	0	1		1+{1}	
		10	-1/3	5	5	5+{5}+[5]	5+[5]
		10	-1	1		1	
		10	-3	1		1	
		10	-∞	1		1	
		15	0	5	5	5+{1}	5
		15	-1/3	5	5	5+{5}+[5]	5+[5]
		15	-1	5	5	5	5
		15	-3	5	5	5	5
		15	-∞	5+(1)	5	5+{1}	5
	10^{-4}	0	-1/3			1	
		5	0	1		1+{1}	
		5	-1/3	1		1+{1}	
		5	-∞	1		1+{1}	
		10	0	1		1+{1}	
		10	-1/3	1		1+{1}	
		10	-∞	1		1+{1}	
		15	0	1		1+{1}	
		15	-1/3	1		1+{1}	
		15	-1	1		1	
		15	-3	1		1	
		15	-∞	1		1+{1}	
	10^{-6}	0	-1/3			1	
		15	-1/3			{1}	
	5×10^{-5}	0	-1/3			1	
		15	-1/3			{1}	

Table D.1: Cases of simulations performed at 1400°C.

				Spherical voids		Polyhedral voids	
T [°C]	$\lvert\dot{E}\rvert$ [s^{-1}]	f_p [%]	T_σ	$d_p \approx d_g$	$d_p \approx 2d_g$	$d_p \approx d_g$	$d_p \approx 2d_g$
1700	10^{-7}	0	-1/3			1	
		5	0	1		1+{1}	
		5	-1/3	1		1+{1}	
		5	-∞	1		1+{1}	
		10	0	1		1+{1}	
		10	-1/3	1		1+{1}	
		10	-∞	1		1+{1}	
		15	0	1		1+{1}	
		15	-1/3	1		1+{1}	
		15	-1	1		1	
		15	-3	1		1	
		15	-∞	1		1+{1}	
	10^{-4}	0	-1/3			1	
		5	0	1		1+{1}	
		5	-1/3	1		1+{1}	
		5	-∞	1		1+{1}	
		10	0	1		1+{1}	
		10	-1/3	1		1+{1}	
		10	-∞	1		1+{1}	
		15	0	1		1+{1}	
		15	-1/3	1		1+{1}	
		15	-1	1		1	
		15	-3	1		1	
		15	-∞	1		1+{1}	
	10^{-6}	0	-1/3			1	
		15	-1/3			{1}	
	5×10^{-5}	0	-1/3			1	
		15	-1/3			{1}	
1550	10^{-7}	0	-1/3			1	
		15	-1/3			{1}	
	10^{-6}	0	-1/3			1	
		15	-1/3			{1}	
	5×10^{-5}	0	-1/3			1	
		15	-1/3			{1}	
	10^{-4}	0	-1/3			1	
		15	-1/3			{1}	

Table D.2: Cases of simulations performed at 1700°C and 1550°C.

References

F. Aurenhammer. Power Diagrams: Properties, Algorithms and Applications. SIAM Journal on Computing, 16(1):78–96, Feb. 1987. doi: 10.1137/0216006. URL https://epubs.siam.org/doi/10.1137/0216006.

F. Aurenhammer. Voronoi diagrams—a survey of a fundamental geometric data structure. ACM Comput. Surv., 23(3): 345–405, Sept. 1991. ISSN 0360-0300. doi: 10.1145/116873.116880. URL https://doi-org.insis.bib.cnrs.fr/10.1145/116873.116880.

C. Bellis and P. Suquet. Geometric Variational Principles for Computational Homogenization. Journal of Elasticity, 137(2): 119–149, 2019. doi: 10.1007/s10659-018-09713-9. URL https://doi.org/10.1007/s10659-018-09713-9.

N. Bilger, F. Auslender, M. Bornert, J.-C. Michel, H. Moulinec, P. Suquet, and A. Zaoui. Effect of a nonuniform distribution of voids on the plastic response of voided materials: a computational and statistical analysis. International Journal of Solids and Structures, 42(2):517–538, 2005. doi: 10.1016/j.ijsolstr.2004.06.048. URL http://www.sciencedirect.com/science/article/pii/S0020768304003452.

P. E. Bohaboy, R. R. Asamoto, and A. E. Conti. Compressive creep characteristics of stoichiometric uranium dioxide. Technical Report GEAP-10054, General Electric, 1969. URL https://digital.library.unt.edu/ark:/67531/metadc1029033/.

G. Boittin, P.-G. Vincent, H. Moulinec, and M. Gărăjeu. Numerical simulations and modeling of the effective plastic flow surface of a biporous material with pressurized intergranular voids. Computer Methods in Applied Mechanics and Engineering, 323:174 – 201, 2017. doi: https://doi.org/10.1016/j.cma.2017.05.004. URL http://www.sciencedirect.com/science/article/pii/S0045782516302705.

B. Burton, G. L. Reynolds, and J. P. Barnes. The influence of grain size on the creep of uranium dioxide. Journal of Materials Science, 8(12):1690–1694, 1973. doi: 10.1007/BF02403517. URL https://link.springer.com/article/10.1007/BF02403517.

J. F. Byron. Yield and flow of polycrystalline uranium dioxide. Journal of Nuclear Materials, 27(1):48–53, 1968. doi: 10.1016/0022-3115(68)90006-8. URL http://www.sciencedirect.com/science/article/pii/0022311568900068.

L. Caillot, C. Nonon, and V. Basini. Out-of-pile and in-pile viscoplastic behaviour of mixed-oxide fuels. Technical report, CEA Cadarache, 2004. URL http://inis.iaea.org/Search/search.aspx?orig_q=RN:37021736.

F. Chen, I. Sevostianov, A. Giraud, and D. Grgic. Evaluation of the effective elastic and conductive properties of a material containing concave pores. International Journal of Engineering Science, 97:60–68, 2015. doi: 10.1016/j.ijengsci.2015.08.012. URL https://www.sciencedirect.com/science/article/pii/S0020722515001299.

F. Chen, I. Sevostianov, A. Giraud, and D. Grgic. Combined effect of pores concavity and aspect ratio on the elastic properties of a porous material. International Journal of Solids and Structures, 134:161–172, 2018. doi: 10.1016/j.ijsolstr.2017.10.016. URL https://www.sciencedirect.com/science/article/pii/S0020768317304778.

R. L. Coble. A Model for Boundary Diffusion Controlled Creep in Polycrystalline Materials. Journal of Applied Physics, 34 (6):1679–1682, 1963. doi: 10.1063/1.1702656. URL https://aip.scitation.org/doi/10.1063/1.1702656.

B. Drach, I. Tsukrov, T. Gross, S. Dietrich, K. Weidenmann, R. Piat, and T. Böhlke. Numerical modeling of carbon/carbon composites with nanotextured matrix and 3D pores of irregular shapes. International Journal of Solids and Structures, 48(18):2447–2457, 2011. doi: 10.1016/j.ijsolstr.2011.04.021. URL https://www.sciencedirect.com/science/article/pii/S0020768311001740.

B. Drach, A. Drach, and I. Tsukrov. Prediction of the effective elastic moduli of materials with irregularly-shaped pores based on the pore projected areas. International Journal of Solids and Structures, 51(14):2687–2695, 2014. doi: 10.1016/j.ijsolstr.2014.03.042. URL http://www.sciencedirect.com/science/article/pii/S0020768314001486.

B. Drach, I. Tsukrov, and A. Trofimov. Comparison of full field and single pore approaches to homogenization of linearly elastic materials with pores of regular and irregular shapes. International Journal of Solids and Structures, 96:48–63, 2016. doi: 10.1016/j.ijsolstr.2016.06.023. URL http://www.sciencedirect.com/science/article/pii/S002076831630138X.

K. Du, L. Cheng, J. F. Barthélémy, I. Sevostianov, A. Giraud, and A. Adessina. Numerical computation of compliance contribution tensor of a concave pore embedded in a transversely isotropic matrix. International Journal of Engineering Science, 152:103306, 2020. doi: 10.1016/j.ijengsci.2020.103306. URL http://www.sciencedirect.com/science/article/pii/S002072252030094X.

K. Du, L. Cheng, J. F. Barthélémy, I. Sevostianov, A. Giraud, and A. Adessina. Effective elastic properties of transversely isotropic materials with concave pores. Mechanics of Materials, 153:103665, 2021. doi: 10.1016/j.mechmat.2020.103665. URL http://www.sciencedirect.com/science/article/pii/S0167663620306980.

T. C. Ekneligoda and R. W. Zimmerman. Compressibility of two-dimensional pores having n-fold axes of symmetry. Proceedings of the Royal Society A: Mathematical, Physical and Engineering Sciences, 462(2071):1933–1947, 2006. doi: 10.1098/rspa.2006.1666. URL https://royalsocietypublishing-org.insis.bib.cnrs.fr/doi/10.1098/rspa.2006.1666.

S. El Shawish, P.-G. Vincent, H. Moulinec, L. Cizelj, and L. Gélébart. Full-field polycrystal plasticity simulations of neutron-irradiated austenitic stainless steel: A comparison between FE and FFT-based approaches. Journal of Nuclear Materials, 529:151927, 2020. doi: 10.1016/j.jnucmat.2019.151927. URL http://www.sciencedirect.com/science/article/pii/S0022311519309845.

S. Evans, P. E. Bohaboy, and R. Laskiewicz. Compressive creep of Uraniu-Plutonia fuels. AEX research and development report GEAP-13732, General Electric, 1971.

S. Fisher, R. White, P. Cook, S. Bremier, R. Corcoran, R. Stratton, C. Walker, P. Ivison, and I. Palmer. Microstructure of irradiated SBR MOX fuel and its relationship to fission gas release. Journal of Nuclear Materials, 306(2):153 – 172, 2002. doi: https://doi.org/10.1016/S0022-3115(02)01247-3. URL http://www.sciencedirect.com/science/article/pii/S0022311502012473.

T. Fuketa. Transient Response of LWR fuels (RIA). In R. J. Konings, editor, Comprehensive Nuclear Materials, pages 579 – 593. Elsevier, Oxford, 2012. ISBN 978-0-08-056033-5.

Y. Guerin. Etude par compression à hautes températures de la déformation plastique du bioxyde d'uranium polycristallin. Journal of Nuclear Materials, 56(1):61–75, 1975. doi: 10.1016/0022-3115(75)90197-X. URL http://www.sciencedirect.com/science/article/pii/002231157590197X.

A. L. Gurson. Continuum Theory of Ductile Rupture by Void Nucleation and Growth: Part I—Yield Criteria and Flow Rules for Porous Ductile Media. Journal of Engineering Materials and Technology, 99(1):2–15, 1977. doi: 10.1115/1.3443401. URL https://asmedigitalcollection.asme.org/materialstechnology/article/99/1/2/403937/Continuum-Theory-of-Ductile-Rupture-by-Void.

X. Haller, Y. Monerie, S. Pagano, and P.-G. Vincent. Effective elastic properties of nanoporous materials with spherical and spheroidal voids [propriétés élastiques effectives des matériaux nanoporeux à cavités sphériques et sphéroïdales]. Materiaux et Techniques, 103(3), 2015. doi: 10.1051/mattech/2015021. URL https://www.scopus.com/inward/record.uri?eid=2-s2.0-84930958926&doi=10.1051%2fmattech%2f2015021&partnerID=40&md5=b1adbba76be03bb29cd7efac20556ade.

X. Haller, Y. Monerie, S. Pagano, and P.-G. Vincent. Elastic behavior of porous media with spherical nanovoids. International Journal of Solids and Structures, 84:99–109, 2016. doi: 10.1016/j.ijsolstr.2016.01.018. URL https://www.scopus.com/inward/record.uri?eid=2-s2.0-84968442918&doi=10.1016%2fj.ijsolstr.2016.01.018&partnerID=40&md5=953755a9477523aa2b78d51786ef4970.

C. Herring. Diffusional Viscosity of a Polycrystalline Solid. Journal of Applied Physics, 21(5):437–445, 1950. doi: 10.1063/1.1699681. URL https://aip.scitation.org/doi/10.1063/1.1699681.

M. Houston, O. Kruger, and W. Pardue. Thermal creep of polycristalline UO_2-PuO_2. Technical Report W-7405-eng-92, Battelle Memorial Institute, 1970.

L. Joëssel, P.-G. Vincent, M. Gărăjeu, and M. Idiart. Viscoplasticity of voided cubic crystals under hydrostatic loading. International Journal of Solids and Structures, 147:156–165, 2018. doi: 10.1016/j.ijsolstr.2018.05.022. URL https://www.scopus.com/inward/record.uri?eid=2-s2.0-85048485824&doi=10.1016%2fj.ijsolstr.2018.05.022&partnerID=40&md5=b31e77434033b18baeda08bf0e5d7cef.

M. Kachanov, I. Tsukrov, and B. Shafiro. Effective Moduli of Solids With Cavities of Various Shapes. Applied Mechanics Reviews, 47(1S):S151–S174, 1994. doi: 10.1115/1.3122810. URL https://doi.org/10.1115/1.3122810.

Y.-H. Koo, D.-S. Sohn, and B. Volkov. A comparative analysis of UO2 and MOX fuel behavior under reactivity initiated accident. Annals of Nuclear Energy, 24(11):859–870, 1997.

C. Lautensack and S. Zuyev. Random Laguerre Tessellations. Advances in Applied Probability, 40(3):630–650, 2008. URL http://www.jstor.org/stable/20443601.

R. Lebensohn, M. Idiart, P. Castañeda, and P.-G. Vincent. Dilatational viscoplasticity of polycrystalline solids with intergranular cavities. Philosophical Magazine, 91(22):3038–3067, 2011. doi: 10.1080/14786435.2011.561811. URL https://www.scopus.com/inward/record.uri?eid=2-s2.0-79959329475&doi=10.1080%2f14786435.2011.561811&partnerID=40&md5=0b3a62acbefb24a1e0ac37306df3782f.

N. Lozano, L. Desgranges, D. Aymes, and J. C. Niepce. High magnification SEM observations for two types of granularity in a high burnup PWR fuel rim. Journal of Nuclear Materials, 257(1):78–87, 1998. doi: 10.1016/S0022-3115(98)00056-7. URL http://www.sciencedirect.com/science/article/pii/S0022311598000567.

A. Markov, A. Trofimov, and I. Sevostianov. A unified methodology for calculation of compliance and stiffness contribution tensors of inhomogeneities of arbitrary 2D and 3D shapes embedded in isotropic matrix – open access software. International Journal of Engineering Science, 157:103390, 2020. doi: 10.1016/j.ijengsci.2020.103390. URL https://www.sciencedirect.com/science/article/pii/S0020722520301774.

H. Moulinec and P. Suquet. A fast numerical method for computing the linear and nonlinear mechanical properties of composites. Les Comptes Rendus de l'Academie des Sciences Paris II, 318(11):1417–1423, 1994.

H. Moulinec and P. Suquet. A numerical method for computing the overall response of nonlinear composites with complex microstructure. Computer Methods in Applied Mechanics and Engineering, 157(1-2):69–94, 1998. doi: 10.1016/S0045-7825(97)00218-1. URL https://www-sciencedirect-com.insis.bib.cnrs.fr/science/article/pii/S0045782597002181.

F. R. N. Nabarro. Deformation of crystals by the motion of single ions. Report of a conference on the strength of solids, Physical Society of London, 1948.

N. Nkoumbou Kaptchouang, Y. Monerie, F. Perales, and P.-G. Vincent. Cohesive GTN model for ductile fracture simulation. Engineering Fracture Mechanics, 242, 2021. doi: 10.1016/j.engfracmech.2020.107437. URL https://www.scopus.com/inward/record.uri?eid=2-s2.0-85097636071&doi=10.1016%2fj.engfracmech.2020.107437&partnerID=40&md5=241b5b3674d4cdad23f473cbde36ea46.

J. Noirot, L. Desgranges, and J. Lamontagne. Detailed characterisations of high burn-up structures in oxide fuels. Journal of Nuclear Materials, 372(2):318 – 339, 2008. doi: https://doi.org/10.1016/j.jnucmat.2007.04.037. URL http://www.sciencedirect.com/science/article/pii/S0022311507006666.

G. Oudinet, I. Munoz-Viallard, L. Aufore, M.-J. Gotta, J. M. Becker, G. Chiarelli, and R. Castelli. Characterization of plutonium distribution in MIMAS MOX by image analysis. Journal of Nuclear Materials, 375(1):86–94, 2008. doi: 10.1016/j.jnucmat.2007.10.013. URL http://www.sciencedirect.com/science/article/pii/S0022311507010501.

L. Portelette. Analyse des mécanismes de glissement des dislocations dans l'UO_2 à l'aide de la modélisation multi-échelles comparée à l'expérience. thesis, Aix-Marseille, 2018. URL http://www.theses.fr/2018AIXM0406.

L. Portelette, J. Amodeo, R. Madec, J. Soulacroix, T. Helfer, and B. Michel. Crystal viscoplastic modeling of UO_2 single crystal. Journal of Nucear Materials, 510:635 – 643, 2018. doi: https://doi.org/10.1016/j.jnucmat.2018.06.035. URL http://www.sciencedirect.com/science/article/pii/S0022311518305981.

L. Portelette, J. Amodeo, B. Michel, and R. Madec. Athermal dislocation strengthening in UO_2. Journal of Nuclear Materials, 538:1–11, 2020. doi: 10.1016/j.jnucmat.2020.152157. URL http://www.sciencedirect.com/science/article/pii/S0022311519316411.

K. C. Radford and G. R. Terwilliger. Compressive Deformation of Polycrystalline UO_2. Journal of the American Ceramic Society, 58(7-8):274–278, 1975. doi: 10.1111/j.1151-2916.1975.tb11474.x. URL https://onlinelibrary.wiley.com/doi/abs/10.1111/j.1151-2916.1975.tb11474.x.

J. Routbort, N. Javed, and J. Voglewede. Compressive creep of mixed-oxide fuel pellets. Journal of Nuclear Materials, 44(3):247–259, 1972. doi: 10.1016/0022-3115(72)90036-0. URL https://linkinghub.elsevier.com/retrieve/pii/0022311572900360.

J. L. Routbort and J. C. Voglewede. Creep of Mixed-Oxide Fuel Pellets at High Stress. Journal of the American Ceramic Society, 56(6):330–333, 1973. doi: 10.1111/j.1151-2916.1973.tb12507.x. URL https://ceramics.onlinelibrary.wiley.com/doi/abs/10.1111/j.1151-2916.1973.tb12507.x.

M. Salvo, J. Sercombe, J.-C. Ménard, J. Julien, T. Helfer, and T. Désoyer. Experimental characterization and modelling of UO2 behavior at high temperatures and high strain rates. Journal of Nuclear Materials, 456:54–67, 2015. doi: 10.1016/j.jnucmat.2014.09.024. URL http://www.sciencedirect.com/science/article/pii/S002231151400614X.

H. Sasajima, T. Fuketa, T. Nakamura, J. Nakamura, and K. Kikuchi. Behavior of irradiated ATR/MOX fuel under reactivity initiated accident conditions. Journal of Nuclear Science and Technology, 37(5):455–464, 2000.

F. Schmitz and J. Papin. High burnup effects on fuel behaviour under accident conditions: the tests CABRI REP-Na. Journal of Nuclear Materials, 270(1):55–64, 1999. doi: 10.1016/S0022-3115(98)00895-2. URL http://www.sciencedirect.com/science/article/pii/S0022311598008952.

M. S. Seltzer, A. H. Clauer, and B. A. Wilcox. The stress dependence for high temperature creep of polycrystalline uranium dioxide. Journal of Nuclear Materials, 34(3):351–353, 1970. doi: 10.1016/0022-3115(70)90206-0. URL http://www.sciencedirect.com/science/article/pii/0022311570902060.

M. S. Seltzer, J. S. Perrin, A. H. Clauer, and B. A. Wilcox. Review of Creep Behavior of Ceramic Nuclear Fuels. Reactor Technology, 14(2):99–135, 1971. URL https://www.osti.gov/biblio/4728614-review-creep-behavior-ceramic-nuclear-fuels.

I. Sevostianov and A. Giraud. On the Compliance Contribution Tensor for a Concave Superspherical Pore. International Journal of Fracture, 177(2):199–206, 2012. doi: 10.1007/s10704-012-9754-7. URL https://doi.org/10.1007/s10704-012-9754-7.

I. Sevostianov, F. Chen, A. Giraud, and D. Grgic. Compliance and resistivity contribution tensors of axisymmetric concave pores. International Journal of Engineering Science, 101:14–28, 2016. doi: 10.1016/j.ijengsci.2015.12.005. URL https://www.sciencedirect.com/science/article/pii/S0020722515002050.

O. Slagle, F. Bard, B. Gneiting, and J. Thielges. Fuel transient deformation. Nuclear Engineering and Design, 79(3):301 – 307, 1984. doi: https://doi.org/10.1016/0029-5493(84)90045-1. URL http://www.sciencedirect.com/science/article/pii/0029549384900451.

D. Stoyan, W. Kendall, and J. Mecke. Stochastic Geometry and Its Applications. Inorganic Chemistry. Wiley, 1995. ISBN 9780471950998. URL https://books.google.fr/books?id=oFDvAAAAMAAJ.

P. Suquet, H. Moulinec, O. Castelnau, M. Montagnat, N. Lahellec, F. Grennerat, P. Duval, and R. Brenner. Multi-scale modeling of the mechanical behavior of polycrystalline ice under transient creep. Procedia IUTAM, 3:76–90, 2012. doi: 10.1016/j.piutam.2012.03.006. URL https://www-sciencedirect-com.insis.bib.cnrs.fr/science/article/pii/S2210983812000077.

M. Suzuki, T. Sugiyama, and T. Fuketa. Thermal Stress Analysis of High-Burnup LWR Fuel Pellet Pulse-Irradiated in Reactivity-Initiated Accident Conditions. Journal of Nuclear Science and Technology, 45(11):1155–1164, 2008. doi: 10.1080/18811248.2008.9711904. URL https://www.tandfonline.com/doi/abs/10.1080/18811248.2008.9711904.

T. Tachibana, H. Furuya, and M. Koizumi. Dependence on Strain Rate and Temperature Shown by Yield Stress of Uranium Dioxide. Journal of Nuclear Science and Technology, 13(9):497–502, 1976. doi: 10.1080/18811248.1976.9734063. URL https://www.tandfonline.com/doi/abs/10.1080/18811248.1976.9734063.

I. Tsukrov and J. Novak. Effective elastic properties of solids with defects of irregular shapes. International Journal of Solids and Structures, 39(6):1539–1555, 2002. doi: 10.1016/S0020-7683(01)00285-2. URL http://www.sciencedirect.com/science/article/pii/S0020768301002852.

P.-G. Vincent, Y. Monerie, and P. Suquet. Porous materials with two populations of voids under internal pressure: I. instantaneous constitutive relations. International Journal of Solids and Structures, 46(3-4):480–506, 2009.

P.-G. Vincent, S. Bourgeois, and Y. Monerie. Overall elastoplastic behavior of anisotropic metal-matrix composites reinforced by aligned inclusions. application to hydrided and irradiated zircaloy-4 cladding tubes. Mechanics of Materials, 42(2):175–188, 2010. doi: 10.1016/j.mechmat.2009.11.004. URL https://www.scopus.com/inward/record.uri?eid=2-s2.0-73549101504&doi=10.1016%2fj.mechmat.2009.11.004&partnerID=40&md5=5e48d227533af75fa5e30a522a4fd80a.

P.-G. Vincent, H. Moulinec, L. Joëssel, M. Idiart, and M. Gărăjeu. Porous polycrystal plasticity modeling of neutron-irradiated austenitic stainless steels. Journal of Nuclear Materials, 542, 2020. doi: 10.1016/j.jnucmat.2020.152463. URL https://www.scopus.com/inward/record.uri?eid=2-s2.0-85090875836&doi=10.1016%2fj.jnucmat.2020.152463&partnerID=40&md5=80166a8b289df2d3b21a34091088552d.

J. B. Wachtman, M. L. Wheat, H. J. Anderson, and J. L. Bates. Elastic constants of single crystal UO2 at 25° C. Journal of Nuclear Materials, 16(1):39–41, 1965. doi: 10.1016/0022-3115(65)90089-9. URL http://www.sciencedirect.com/science/article/pii/0022311565900899.

R. J. White, S. B. Fisher, P. M. A. Cook, R. Stratton, C. T. Walker, and I. D. Palmer. Measurement and analysis of fission gas release from BNFL's SBR MOX fuel. Journal of Nuclear Materials, 288(1):43–56, 2001. doi: 10.1016/S0022-3115(00)00591-2. URL https://www.sciencedirect.com/science/article/pii/S0022311500005912.

K. Wojtacki, P.-G. Vincent, P. Suquet, H. Moulinec, and G. Boittin. A micromechanical model for the secondary creep of elasto-viscoplastic porous materials with two rate-sensitivity exponents: Application to a mixed oxide fuel. International Journal of Solids and Structures, 184:99 – 113, 2020. doi: https://doi.org/10.1016/j.ijsolstr.2018.12.026. URL http://www.sciencedirect.com/science/article/pii/S0020768318305237.

R. W. Zimmerman. Compressibility of Two-Dimensional Cavities of Various Shapes. Journal of Applied Mechanics, 53(3):500–504, 1986. doi: 10.1115/1.3171802. URL https://doi.org/10.1115/1.3171802.